Heliyon 10 (2024) e28821

Contents lists available at ScienceDirect

Heliyon

journal homepage: www.cell.com/heliyon

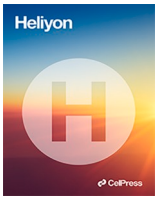

Research article

Spatiotemporal development of the neuronal accumulation of amyloid precursor protein and the amyloid plaque formation in the brain of 3xTg-AD mice

Munenori Ono [a,*], Tetsufumi Ito [b], Sachiko Yamaki [a], Yoshie Hori [a], Qing Zhou [a], Xirun Zhao [a], Shinji Muramoto [a], Ryo Yamamoto [a], Takafumi Furuyama [a], Hiromi Sakata-Haga [c], Toshihisa Hatta [c], Tsuyoshi Hamaguchi [d], Nobuo Kato [a]

[a] Department of Physiology, Kanazawa Medical University, Ishikawa, 920-0293, Japan
[b] Systems Function and Morphology, University of Toyama, Toyama, 930-0194, Japan
[c] Department of Anatomy, Kanazawa Medical University, Ishikawa, 920-0293, Japan
[d] Department of Neurology, Kanazawa Medical University, Ishikawa, 920-0293, Japan

ARTICLE INFO

Keywords:
Alzheimer's disease
Amyloid precursor protein
β-amyloid
Immunohistochemistry
Transgenic animal

ABSTRACT

The amyloid plaque is a hallmark of Alzheimer's disease. The accumulation of the amyloid precursor protein (APP) in the neuronal structure is assumed to lead to amyloid plaque formation through the excessive production of β-amyloid protein. To study the relationship between the neuronal accumulation of APP and amyloid plaque formation, we histologically analyzed their development in the different brain regions in 3xTg-AD mice, which express Swedish mutated APP (APP_{SWE}) in the neurons. Observation throughout the brain revealed APP_{SWE}-positive somata in the broad regions. Quantitative model analysis showed that the somatic accumulation of APP_{SWE} developed firstly in the hippocampus from a very early age (<1 month) and proceeded slower in the isocortex. In line with this, the hippocampus was the first region to form amyloid plaques at the age of 9–12 months, while amyloid plaques were rarely observed in the isocortex. Females had more APP_{SWE}-positive somata and plaques than males. Furthermore, amyloid plaques were observed in the lateral septum and pontine grey, which did not contain APP_{SWE}-positive somata but only the APP_{SWE}-positive fibers. These results suggested that neuronal accumulation of APP_{SWE}, both in somatodendritic and axonal domains, is closely related to the formation of amyloid plaques.

1. Introduction

Alzheimer's disease (AD) is the main cause of dementia, and more than 50 million people are estimated to have AD worldwide [1]. The formation of extracellular amyloid plaques and intracellular neurofibrillary tangles characterizes AD. The former mainly consists of β-amyloid, a small peptide of 36–43 amino acids derived from amyloid precursor protein (APP), and the latter is caused by hyperphosphorylated tau protein. Accumulation of β-amyloid is known to induce neuronal dysfunction [2] and is supposed to cause cognitive impairment in AD. β-amyloid first forms soluble neurotoxic oligomers and finally aggregates in the extracellular space to

* Corresponding author. Department of Physiology, School of Medicine, Kanazawa Medical University, Uchinada, Ishikawa, 920-0293, Japan.
E-mail address: onomn@kanazawa-med.ac.jp (M. Ono).

https://doi.org/10.1016/j.heliyon.2024.e28821
Received 28 August 2023; Received in revised form 25 March 2024; Accepted 25 March 2024
Available online 30 March 2024

Abbreviations

V	motor nucleus of trigeminal
VII	facial motor nucleus
XII	hypoglossal nuicleus
ACA	anterior cingulate area
ACB	nucleus accumbens
AD	Alzheimer's disease
AI	agranular insular area
AON	anterior olfactory nucleus
APP	amyloid precursor protein
AUD	auditory area
BLA	basolateral amygdala
BST	bed nuclei of stria terminalis
CBN	cerebellar nuclei
CBX	cerebellar cortex
CLA	claustrum
CN	cochlear nuclei
COA	cortical amygdalar area
CP	caudoputamen
cpd	cerebal peduncle
CU	cuneate nucleus
DG	dentate gyrus
DP	dorsal peduncular area
ECT	ectorhinal area
ECU	external cuneate nucleus
ENT	entorhinal cortex
EP	endopiriform nucleus
GP	globus pallidus
GRN	gigantocellular reticular nucleus
GU	gustatory area
HY	hypothalamus
IC	inferior colliculus
ILA	infralimbic area
IO	inferior olive
IRN	intermediate reticular nucleus
ISO	isocortex
LRN	lateral reticular nucleus
LS	lateral septal nucleus
MEV	midbrain trigeminal nucleus
MARN	magnocellular reticular nucleus
mlf	medial longitudinal fascicle
MO	motor area
MOB	main olfactory bulb
MRN	midbrain reticular nucleus
MS	medial septal nucleus
NTS	nucleus of solitary tract
ORB	orbital area
PAG	periaqueductal grey
PAR	parasubiculum
PARN	parvicellular reticular nucleus
PB	parabrachial nucleus
PCG	pontine central grey
PERI	perirhinal area
PGRN	paragigantocellular reticular nucleus
PIR	piriform area
PL	prelimbic area
PRE	presubiculum
PRN	pontine reticular nucleus
PSV	principal sensory nucleus of trigeminal

form amyloid plaques. Thus, the formation of amyloid plaques is a critical hallmark to indicate the sustained high concentration of neurotoxic β-amyloid in the brain. β-amyloid is generated through sequential cleavage of APP by β- and γ-secretase and includes a variety of different lengths [3]. Among them, 42 amino acid form (β-amyloid 1−42) is known to be strongly aggregative and predominantly contributes to plaque formation [4]. The mutations in APP and/or γ-secretase genes have been reported to cause more accumulation of β-amyloid 1-42 than normal and underlie some familial AD [5]. Thus, various AD model transgenic animals have been produced by introducing mutant APP and/or presenilin-1 (PS1) genes, a subunit of γ-secretase. Among them, a triple transgenic (3xTg) AD model mouse [6], harboring APP_{SWE}, $PS1_{M146V,}$ and tau_{P301L} is a widely used model animal that shows neuropathological hallmarks of AD and cognitive decline [6] in an age-dependent manner. In 3xTg-AD mice, APP_{swe} and Tau_{p301L} are both under the control of the mouse Thy1.2 promoter and are widely expressed in the brain [7,8]. Previous studies have reported that amyloid plaques and neurofibrillary tangles were formed in the brain of 3xTg-AD mice, although their onset times varied among them [6,7,9,10]. Recent studies have shown that amyloid plaques develop in a region-specific manner and first appear in the hippocampus, then followed by the isocortex in the brain of 3xTg-AD mice. The formation of amyloid plaques is closely related to the local accumulation of β-amyloid [11], which causes degeneration of neural circuits [2]. Such region-specificity is likely to depend on the accumulation pattern of APP_{SWE}, the precursor protein of β-amyloid. Since the brain is a collection of regions with different functions that constitute intrinsic connectivity networks, it is important to know which regions in the brain of 3xTg-AD mice accumulate APP_{SWE} over time to understand their cognitive pathology. However, the precise spatiotemporal pattern of APP_{SWE} accumulation remains still unclear in the brain of 3xTg-AD mice.

Here, we studied the distribution of APP_{SWE}-positive neurons in the whole brain of 3xTg-AD mice and quantitatively assessed the developmental time course of somatic APP_{SWE} accumulation in different regions. Our results showed that the APP_{SWE}-positive neurons were broadly distributed in the brain of 3xTg-AD mice: isocortex, hippocampus, olfactory area, amygdala, and many nuclei in the brainstem. Among them, the hippocampus was the region where the APP_{SWE} accumulated somata were densely packed from an early age. On the other hand, in the isocortex, somatic APP_{SWE} accumulation developed slower in layers 5 and 6. In some regions, the amount of APP_{SWE}-positive somata showed sexual dimorphism: females had more APP_{SWE}-positive somata than males. In line with the APP_{SWE} accumulation patterns, the amyloid plaques were first observed in the hippocampus and were more abundant in females than males. However, intriguingly, amyloid plaques were also observed in regions with no APP_{SWE}-positive somata but only APP_{SWE}-positive fibers. These results suggested that APP_{SWE} accumulation in the local neuronal circuits could be closely related to the formation of amyloid plaques. A substantial amount of β-amyloid would likely be released from axon terminals.

2. Materials and Methods

All experiments were approved by the Animal Care Committee of Kanazawa Medical University (the ethics approval number: 2023-28) and done in accordance with the guiding principles of the Physiological Society of Japan. All efforts were made to minimize the number of animals used and their suffering.

Animals. 3xTg-AD model mice with Sv129/C57B6 background [6] were obtained in 2008 from Dr. F. M. LaFerla (University of California, Irvine) by way of Dr. Ohyagi's Lab (Kyushu University, Japan). Sv129/C57B6 mice were used as control animals. The animals were kept in group cages under automatic day-night control (12:12h) and allowed free access to food and water.

Antibodies. In this study, we used four antibodies to detect human APP (rat anti-human APP antibody clone1D1, Sigma-Aldrich, catalog#MABN2287, St.Louis, MO), human APP and its fragments (mouse anti- β-amyloid 6E10 antibody, Biolegend, catalog#803004, San Diego, CA), β-amyloid 1-40 (rabbit anti-β-amyloid 1-40 antibody, Invitrogen, catalog#44-136, Waltham, MA) and

PTL	posterior parietal area
py	pyramid
RM	nucleus raphe magnus
RN	red nucleus
RO	nucleus raphe obscurus
RSP	retrosplenial area
SC	superior colliculus
SI	substantia innominata
SN	substantia nigra
SOC	superior olivary complex
SS	somatosensory area
SUB	subiculum
SUT	supratrigeminal nucleus
TEa	temporal association area
TH	thalamus
TT	taenia tecta
VIS	visual area
VISC	visceral area
VNC	vestibular nuclei
VTA	ventral tegmental area

β-amyloid 1-42 (rabbit anti-β-amyloid1-42 antibody, Sigma-Aldrich, catalog#AB5078P). The amino acid sequence of the antigen for each antibody is described in Supplementary Fig. 1B. The rat anti-human APP antibody 1D1 recognizes the amino acid sequence (Supplementary Fig. 1B) in the human APP's N-terminal E1 domain (Supplementary Fig. 1A). Thus, it does not recognize C-terminal APP fragments and β-amyloid. In contrast, the mouse anti- β-amyloid 6E10 antibody recognizes the amino acid sequence (Supplementary Fig. 1B) in the β-amyloid domain (Supplementary Fig. 1A) in the human APP. Thus, the mouse anti- β-amyloid 6E10 antibody binds to full-length human APP, the C-terminal fragments of APP, and β-amyloid. The specificity of rat anti-human APP antibody 1D1 and mouse anti- β-amyloid 6E10 antibody was evaluated by Western blot analysis and immunoprecipitation [12]. Both antibodies were specific for human APP and showed no cross-reaction with mouse APP. The rabbit anti-β-amyloid 1-40 and anti-β-amyloid 1-42 antibodies had no cross-reaction for β-amyloid 1-42 and β-amyloid1-40, respectively (according to the manufacturer's information).

Histology. We used 38 transgenic mice (3xTg-AD mice) of 0.5–12-month-old (male, N = 17, female, N = 21). Animals were deeply anesthetized with pentobarbital sodium (150 mg/1 kg, i.m.). The mice were transcardially perfused with 4% paraformaldehyde in 0.1 M phosphate buffer (pH 7.4). The brains were dissected and post-fixed overnight in 4% paraformaldehyde at 4 °C. After cryoprotection with 30% (w/w) sucrose in 0.1 M phosphate buffer (pH 7.4, cryoprotection solution), the brain was embedded in gelatin. First, the brain was incubated overnight in 12.5% gelatin (w/w) in a cryoprotection solution at 38 °C. Next, the brain was incubated overnight in 25% (w/w) gelatin in a cryoprotection solution at 38 °C. Then, the brain covered with gelatin was cooled in a refrigerator (4 °C) for 15 min and fixed overnight in 4% formaldehyde in cryoprotection solution at 4 °C. After the fixation, the gelatin-embedded brain was cryoprotected and cut into 40-μm-thick coronal sections on a freezing microtome from the olfactory bulb to the medulla. Every six sections were collected in separate wells and used for histology.

For bright-field immunohistochemistry (IHC), sections were incubated for 2 h with 0.1 M citrate buffer (pH 6.0) at 80 °C for heat-induced epitope retrieval (HIER). After HIER, the endogenous peroxidase activity was quenched by incubation with 0.1 % H_2O_2 in 10 mM PBS for 15 min. Then sections were incubated overnight with either rat anti-human APP antibody (1:500) or mouse anti-β-amyloid 6E10 (1:1000) or rabbit anti-β-amyloid 1-40 (1:500), rabbit anti-β-amyloid 1-42 (1:500), diluted in incubation buffer (1% normal donkey serum, 0.3% Triton X-100, 0.2% sodium azide, and 10 mM PBS) at room temperature. For β-amyloid 1-42 staining to visualize the amyloid plaques, the sections were incubated in 88% formic acid for 30 min after HIER. After the primary antibody incubation, sections were washed and incubated with donkey biotinylated anti-rat or anti-mouse IgG or anti-rabbit IgG (1:200; Jackson ImmunoResearch, West Grove, PA) for 3 h. Then, the sections were washed and incubated for 1 h with avidin-biotinylated horseradish peroxidase complex (1:50; ABC Elite, Vector Laboratories, Burlingame, CA, USA) and visualized with nickel-diaminobenzidine (Ni-DAB) procedure for 5–15 min. The mounted sections were dehydrated, cleared with xylene, and cover-slipped with Entellan (Merck, Whitehouse Station, NJ). In addition to these stainings, the neighboring sections were Nissl-stained to confirm cytoarchitecture.

For fluorescent IHC for human APP 1D1 and β-amyloid 6E10, after HIER, the sections were incubated overnight with rat anti-human APP antibody 1D1 (1:250) and mouse anti- β− amyloid6E10 (1:500) diluted in incubation buffer at room temperature. Next, the sections were washed and incubated with donkey AlexaFluor488-conjugated anti-mouse IgG (1:200; Jackson ImmunoResearch) and donkey AlexaFluor594-conjugated anti-rat IgG (1:200; Jackson ImmunoResearch) for 2 h. For fluorescent IHC for human APP 1D1, β-amyloid 1-42, and Thioflavin-S, after HIER and formic acid treatment, the sections were incubated overnight with rat anti-human APP antibody 1D1 (1:200) and rabbit anti- β-amyloid 1-42 (1:200) diluted in incubation buffer at room temperature. Next, the sections were washed and incubated with donkey AlexaFluor594-conjugated anti-rat IgG (1:200; Jackson ImmunoResearch) and donkey Cy5-conjugated anti-rabbit IgG (1:200; Jackson ImmunoResearch) for 2 h. Then, the sections were washed and fixed with 4% formaldehyde for 10 min. After washing, the sections were incubated with 0.5% Thioflavin-S (Sigma-Aldrich) diluted in 50% ethanol for 10 min. Then the sections were washed twice in 50% ethanol for 5 min and in PBS for 10 min. Cross-reactions of secondary antibodies were examined for the double labeling of human APP 1D1 and β-amyloid 6E10 by omitting the rat or mouse antibody in the primary incubation. We found no significant cross-reactivities of the secondary antibodies to lead to false positive double labeling. We also checked the background staining of the secondary antibodies by omitting the primary antibodies and found that the background did not lead to false positive double labeling.

For fluorescent IHC, the mounted sections were incubated in $CuSO_4$ solution (1 mM $CuSO_4$ in 50 mM ammonium acetate, pH 5.0) for 1 h to reduce the lipofuscin-like autofluorescence. After washing, the sections were over-slipped with 1,4-diazabicyclo[2.2.2]octane. The double-stained sections for APP1D1 and 6E10 were imaged with a structured illumination fluorescent microscope (AxioImager.M2 plus Apotome.2, Carl Zeiss Microscopy, Jena, Germany) equipped with a 20 × lens (NA = 0.8) using tile scanning. The triple-stained sections for APP1D1, β-amyloid 1-42, and Thioflavin-S were imaged with a laser scanning confocal microscope (LSM 700, Zeiss). For broad-area image acquisition, tiled images were obtained with a 40 x oil-immersion lens (NA = 1.3). Tile scanning was taken at 6 μm increments along the z-axis for the entire thickness of the sections. Individual plaques were imaged with a 63 x oil-immersion lens (NA = 1.4) at 3 μm increments along the z-axis. Alexa Fluor 488 and Thioflavin-S were excited by a 488-nm Ar laser, and the emitted fluorescence was filtered with a 493- to 556-nm bandpass filter. Alexa Fluor 594 was excited by a 561 nm.

The diode-pumped solid-state laser and the emitted fluorescence were filtered with a 589- to 628-nm bandpass filter. Cy5 was excited by a 633-nm He–Ne laser, and emitted fluorescence was filtered with a 643- to 759-nm low-pass filter. Images of each dye were taken sequentially to avoid bleed-through artifacts.

Analysis. To classify the mouse brain regions, we followed the nomenclature of Allen Brain Atlas (https://portal.brain-map.org/). To quantitatively analyze the somatic accumulation of APP_{SWE}, we counted the number of neuronal somata positive for human APP 1D1 or β-amyloid 6E10. The APP_{SWE}-positive somata in the isocortex and entorhinal cortex were counted using Neurolucida software (MBF Bioscience, Williston, VT) and a motorized upright microscope (BX-51, Olympus, Tokyo, Japan) equipped with a digital camera (QICAM, QImaging, Surrey, Canada)with low NA lens. In the hippocampus, the density of positive somata was too high to analyze with a low NA lens. To this end, we employed the optical dissector method using Stereo Investigator software (MBF Bioscience) and the

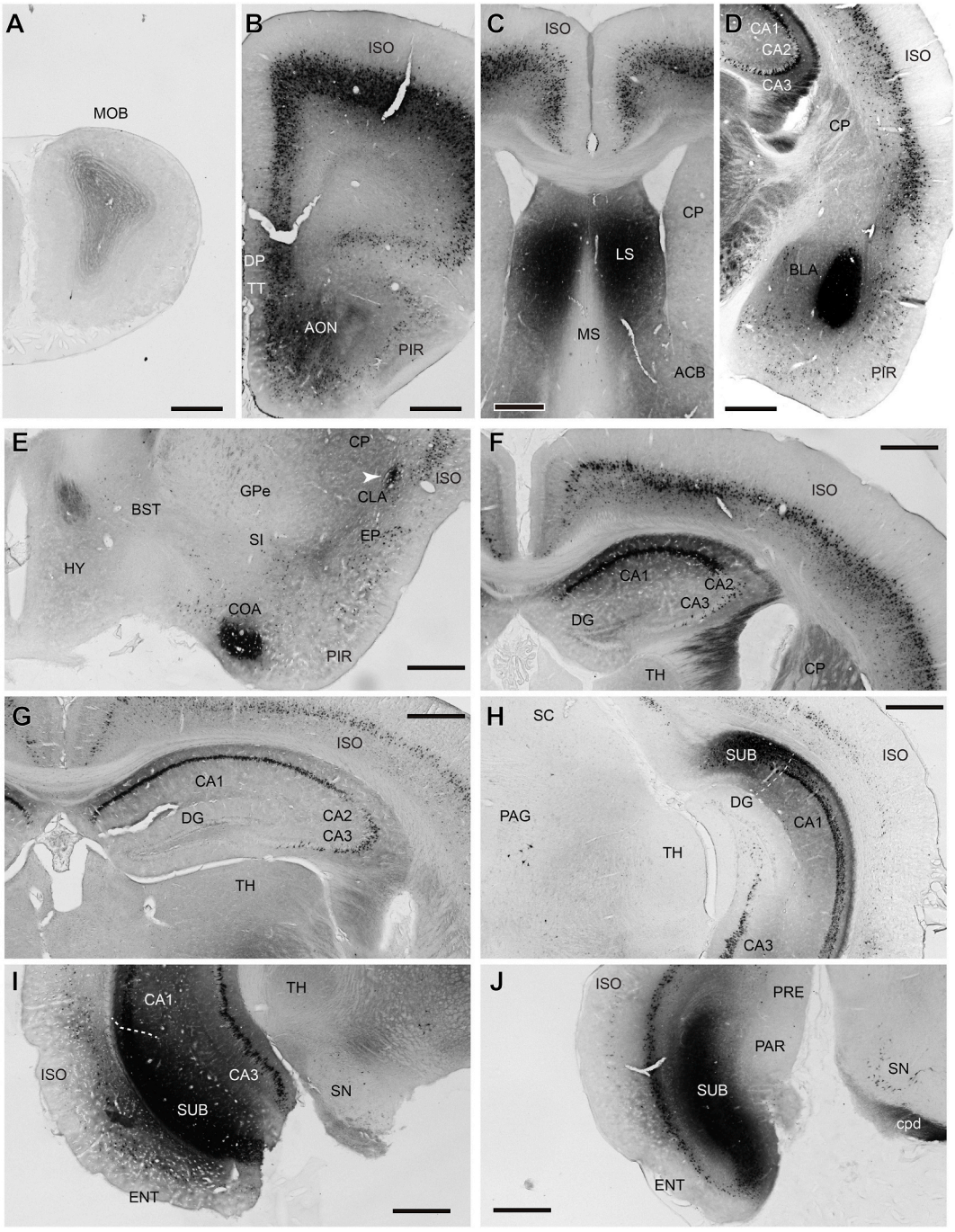

Fig. 1. (A–P) Distribution of the APP_{SWE}-positive neurons in the brain of 3xTg-AD mice. APP_{SWE} was visualized by anti-human APP antibody 1D1. The sections were obtained from 9-month-old female 3xTg-AD mice. Scale bar: 500 μm. Arrowheads in E and N indicate claustrum and cerebellum nuclei, respectively. The white dotted lines in H and I indicate the boundary between the CA1 and subiculum. G and H were obtained from one animal, and other images were obtained from another. To make the boundaries of the hippocampal structures easier to understand, G and H were subjected to the DAB reaction for a shorter time (5 min) than the sections used in the other images (15 min). (Q–T) Details of the APP_{SWE}-positive neurons at higher magnification from the isocortex. (Q, R) and hippocampus (S, T). The photos of the isocortex show a wide area (left) and a magnified (right) image. The arrows indicate the apical dendrites. The photos of the hippocampus show only a wide area. (Q) Motor cortex. (R) Somatosensory cortex. (S) Dorsal CA1. (T) Dorsal CA3. Scale bar in a wide area: 200 μm. Scale bar in a magnified image: 20 μm. (U, V) The images of double labeling (left panels) by anti-human APP antibody 1D1 (right panels) and anti- β-amyloid 6E10 antibody (middle panels). (U) isocortex. (V) the pyramidal layer in the dorsal CA1. The data were obtained from 12-month-old female mice. Scale bar: 20 μm. Abbreviations are as follows: V, motor nucleus of trigeminal; VII, facial motor nucleus; XII, hypoglossal nuicleus; ACB, nucleus accumbens; AON, anterior olfactory nucleus; BLA, basolateral amygdala; BST, bed nuclei of stria terminalis; CBN, cerebellar nuclei; CBX, cerebellar cortex; CLA, claustrum; COA, cortical amygdalar

area; CP, caudoputamen; cpd, cerebal peduncle; CN, cochlear nuclei; CU, cuneate nucleus; DG, dentate gyrus; DP, dorsal peduncular area; ECU, external cuneate nucleus; ENT, entorhinal cortex; EP, endopiriform nucleus; GP, globus pallidus; GRN, gigantocellular reticular nucleus; HY, hypothalamus; IC, inferior colliculus; IO, inferior olive; ISO, isocortex; IRN, intermediate reticular nucleus; ISO, isocortex; LRN, lateral reticular nucleus; LS, lateral septal nucleus; MARN, magnocellular reticular nucleus; MEV, midbrain trigeminal nucleus; MOB, main olfactory bulb; mlf, medial longitudinal fascicle; MRN, midbrain reticular nucleus; MS, medial septal nucleus; NTS, nucleus of solitary tract; PAG, periaqueductal grey; PAR, parasubiculum; PB, parabrachial nucleus; PCG, pontine central grey; PARN, parvicellular reticular nucleus; PGRN, paragigantocellular reticular nucleus; PIR, piriform area; PRE, presubiculum; PRN, pontine reticular nucleus; PSV, principal sensory nucleus of trigeminal; py, pyramid; RM, nucleus raphe magnus; RN, red nucleus; RO, nucleus raphe obscurus; SC, superior colliculus; SI, substantia innominata; SOC, superior olivary complex; SN, substantia nigra; SUB, subiculum; SUT, supratrigeminal nucleus; TH, thalamus; TT, taenia tecta; VNC, vestibular nuclei; VTA, ventral tegmental area. (For interpretation of the references to color in this figure legend, the reader is referred to the Web version of this article.)

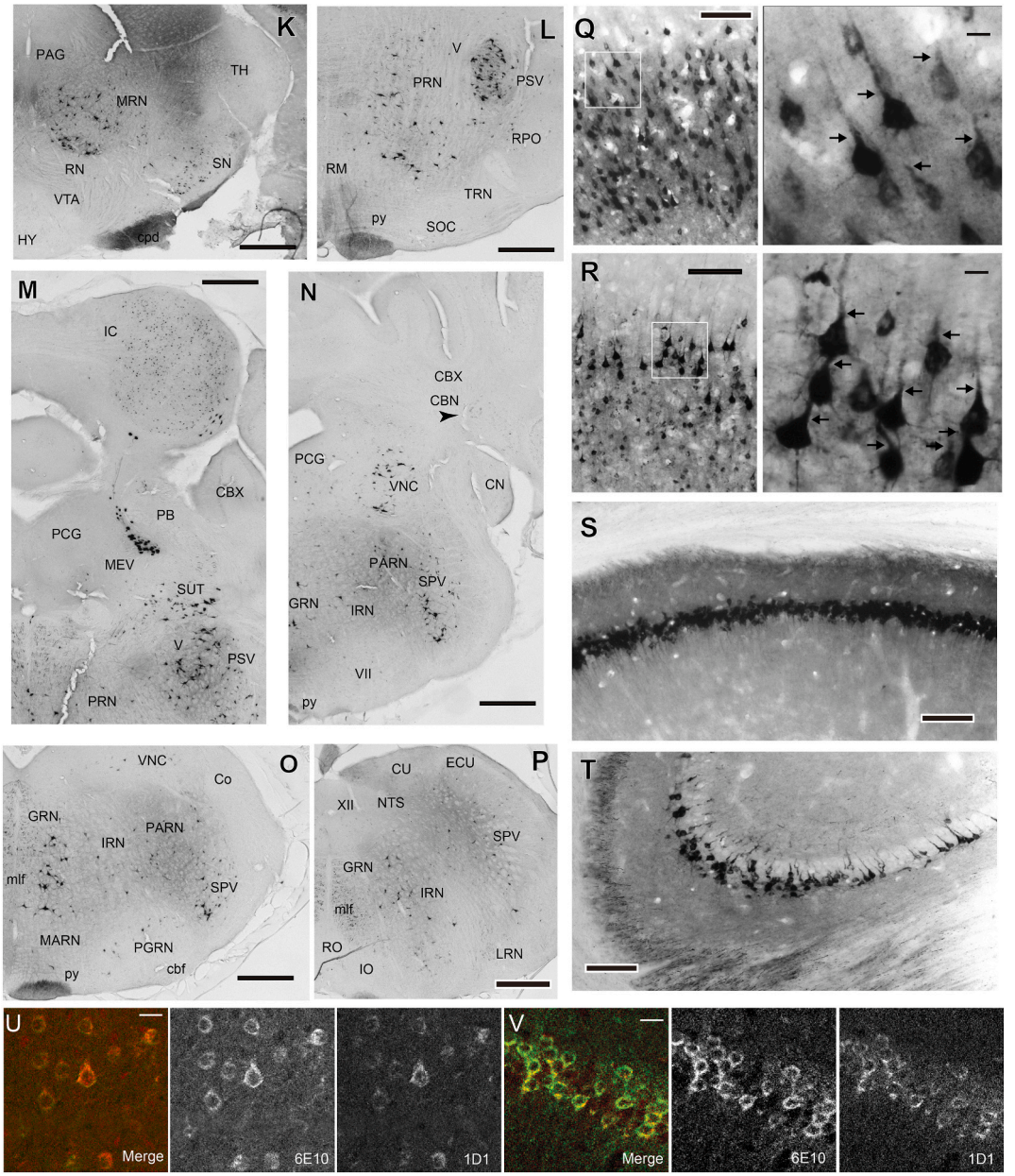

Fig. 1. (*continued*).

motorized microscope with a higher NA lens. For counting with Neurolucida, we first outlined the section under the x2 objective lens (NA = 0.05) and plotted the positions of β-amyloid 6E10 positive somata under the x10 objective lens (NA = 0.4).

After plotting the positive somata in a section was finished, the outline drawing was merged with the image of the corresponding

Table 1
Distribution of the human APP 1D1-positive somata.[a].

Region	the amount of stained somata	Region	the amount of stained somata
Isocortex	++~+++	Retrohippocampal region	
Olfactory areas		Entorhinal area	
Main olfactory bulb	±	Layer1	–
Glomerular layer	±	Layer2	+
External plexiform layer	–	Layer3	+
Mitral cell layer	–	Layer4	++
Accessory olfactory bulb	–	Layer6	++
Anterior olfactory nucleus	++++	Subiculum	+++
Taenia Tecta	+++	Presubiculum	–
Dorsal penducular area	+++	Parasubiculum	–
Piriform area		Postsubiculum	–
Layer1	–	***Cortical subplate***	
Layer2	+	Claustrum	++
Layer3	++	Endopiriform nucleus	++
Nucleus of the lateral olfactory tract	–	Lateral amygdalar nucleus	–
Cortical amygdala area	++++	Basolateral amygdalar nucleus	++++
Piriform amygdala area	+	Basomedial amygdalar nucleus	+
Postpiriform transition area	+	Posterior amygdalar nucleus	+
Hippocampal formation		***Striatum***	
Hippocampal region		Caudate-putamen	–
Ammon's horn		Accumbens nucleus	–
CA1, stratum oriens	–	Olfactory tubercle	±
CA1, stratum pyramidale	++++	Islands of Calleja	–
CA1, stratum radiatum	–	Lateral septal complex	–
CA1, stratum lacunosum-moleculare	–	Striatum-like amygdalar area	
CA2, stratum oriens	–	Anterior amygdalar area	++
CA2, stratum pyramidale	+	Bed nucleus of the accessory olfactory tract	+
CA2, stratum radiatum	–	Central amygdalar nucleus	+
CA2, stratum lacunosum-moleculare	–	Medial amygdalar nucleus	+
CA3, stratum oriens	–	***Pallidum***	
CA3, stratum pyramidale	+++	Globus pallidus	–
CA3, stratum radiatum	–	Medial septal complex	±
CA3, stratum lacunosum-moleculare	–	Triangular nucleus of septum	–
Dentate gyrus		Substantia innominate	+
Molecular layer	–	Magnocellular nucleus	–
Granular layer	+	Bed nucleus of stria terminals	+
Polymorph layer	±~++	***Thalamus***	–
Fasciola cinereia	–	***Hypothalamus****	–
Induseum griseum	–	*only in lateral preoptic area	+

Region	the amount of stained somata	Region	the amount of stained somata
Midbrain, sensory related		***Cerebellar region***	
Inferior colliculus	++	Deep cerebellar nuclei	
Midbrain trigeminal nucleus	++	Fastigial nucleus	++
Midbrain, motor related		Interposed nucleus	++
Substantia nigra, reticular part	+~++	Dentate nucleus	++
Ventral tegmental area	+	***Medulla, sensory related***	
Midbrain reticular nucleus	+	Cuneate nucleus	±
Superior colliculus, motor related		External cuneate nucleus	±
Intermediate grey layer	++	Nucleus of the trapezoid body	±
Intermediate white layer	+	Nucleus of the solitary tract	±
Deep grey layer	+	Spinal nucleus of the trigeminal	
Periaquedal grey	+	Oral part	++
Anterior pretectal nucleus	+	Interpolar part	++
Nucleus of the optic tract	±	Caudal part	++
Cuneiform nucleus	+	***Medulla, motor related***	
Red nucleus	++	Abducens nucleus	++
Oculomotor nucleus	++	Facial motor nucleus	++
Edinger-Westphal nucleus	+	Gigantcellular reticular nucleus	++
Trochlear nucleus	++	Lateral reticular nucleus	±
Pons, sensory related		Magnocellular reticular nucleus	+
Nucleus of lateral lemniscus	++	Medullary reticular nucleus	+
Principal sensory nucleus of the trigeminal	+	Vestibular nuclei	
Superior olivary complex	++	Lateral vestibular nucleus	++
Pons, motor related		Medial vestibular nucleus	±
Pontine central grey	+	Spinal vestibular nucleus	++
Pontine grey	+	Superior vestibular nucleus	++
Supratrigeminal nucleus	+	Hypoglossal nucleus	+

(*continued on next page*)

Table 1 (*continued*)

Region	the amount of stained somata	Region	the amount of stained somata
Motor nucleus of trigeminal	++	***Medulla, behavioral state related***	
Pons, behavioral related		Nucleus raphe magnus	±
Pontine reticular nucleus	++		

[a] The amount of stained somata in different regions was evaluated using internal standards as follows: CA1, stratum pyramidale (++++), subiculum (+++), red nucleus (++), and pontine central grey (+) at 6–12 months old animals. ±, almost negative. -, negative. For the brainstem, only the positive regions were shown.

Nissl-stained section. Observing the merged Nissl-stained section, cortical areas, and layers were specified and added to the outline drawing. The number of APP_{SWE}-positive somata per area in each region was calculated from the data obtained from at least three slices. Neurolucida data was analyzed and visualized with custom-made software written in MATLAB (MathWorks, Natick, MA). For counting with Stereo Investigator, we used an x40 objective lens (NA = 0.85). The regions of interest (ROIs) were divided with sampling frames with a 30 x 30 or 50 × 50 μm. A sampling frame had two inclusion lines and two exclusion lines. The top 5 μm of the section were reserved as guard zones. The dissector height was set at 20 μm. For each ROI, we counted APP_{SWE}-positive somata in sampling frames until Scheaffer's estimated coefficient of error reached below 0.1. Stereological data were exported as Excel files and analyzed using custom-made MATLAB scripts. For quantitative analysis for hippocampus, to reduce variability due to differences in the location of the brain regions to be analyzed, analysis of the anterior hippocampus, posterior hippocampus, and posterior subiculum was limited to areas restricted within the anterior-posterior axis: The anterior hippocampus ranged from −1.955 mm to −2.355 mm from bregma, the posterior hippocampus from −3.18 mm to −3.455 mm, and the posterior subiculum from −3.98 mm to −4.155 mm. We chose the anterior and posterior hippocampi in these ranges because they did not include the subiculum and CA2, respectively, whose boundaries were sometimes difficult to determine.

The size of amyloid plaques was assessed in Ni-DAB developed sections immunostained for 1-42. To evaluate the size of amyloid plaques, the images covering a whole section were acquired with an x4 objective lens using an all-in-one microscope (BZ-9000, Keyence, Osaka, Japan), and a montage of the section was made. Then, the area of the amyloid plaques in the section was measured using ImageJ software (NIH, Bethesda, MD).

Fluorescent images were analyzed and processed using ImageJ.

Statistics. Statistical analysis was performed using R (version 4.1.2) and RStudio (version. 2021.09.1). Values are expressed as mean ± SD unless otherwise indicated. We use N and n for the number of animals and cells, respectively.

We examined the relationship between the number of APP_{SWE}-positive somata per area or the density of APP_{SWE}-positive somata and age using the Bayesian modeling method. The data were fitted with the hierarchical logistic growth curve model as follows.

$$y \sim \mathrm{Norm}\left(\frac{a}{1 + b * exp\left(\frac{-x}{t}\right)}, \sigma^2\right)$$

where y is the number of cells per area or cell density, x is age, σ is standard deviation, and a, b, and τ are constants for logistic growth function. Norm(μ, σ^2) indicates a Gaussian distribution with mean μ and variance σ^2. For a, b, and τ, we examined the models with the region- and/or sex-effects. These effects were obtained by adding the region- or sex-dependent variables to these parameters. For example, parameter a with the region- and sex-effects are written as follows:

$$a = a_0 + a_r + a_s$$

where a_0 is a constant for a, a_r is a variable for regions, and a_s is a variable for females and males. These parameters were estimated by the Markov Chain Monte-Carlo (MCMC) method using R (https://www.r-project.org/) and CmdStanR (https://mc-stan.org/cmdstanr/). For MCMC sampling, four chains were run with 1000 samplings after 1000 warmups. The convergence of the parameters was assessed by the value of Rhat (<1.1). Also, the model was allowed only when less than 1% of samplings (40/4000) were ended with a divergence. In addition to these analyses, the relationship between the position in the anterior-posterior axis and the number of APP_{SWE}-positive somata per area was examined using the Bayesian modeling method. In this analysis, the data were fitted with a linear model with sex-effect.

3. Results

The distribution of the APP_{SWE}*-positive neurons in the central nervous system (CNS).* We first examined the overall distribution of APP_{SWE}-positive neurons in the CNS. To visualize the human-derived APP_{SWE} in the brain of 3xTg-AD animals, we used the antibody for the human APP 1D1 [12]. We found that the antibody stained various brain regions (Fig. 1): isocortex (Fig. 1B–J, Q, R), olfactory areas (Fig. 1B–D, E), hippocampal formation (Fig. 1D, F-J), claustrum (Fig. 1E), basolateral amygdalar nucleus (Fig. 1D), several regions in striatum and pallidum (Fig. 1E), cerebellar nuclei (Fig. 1N) and many nuclei in the midbrain and hindbrain (Fig. 1H-P). In these regions, the neuronal somata and fibers were stained (Figs. 1, 6). The distribution of APP_{SWE}-positive somata in different brain regions was semiquantitatively evaluated in Table 1.

3.1. Isocortex and hippocampal formation

In the isocortex, APP_{SWE}-positive somata were widely distributed through all the regions (Fig. 1B–J). They were primarily distributed in layers 5 and 6 (Fig. 1B–J). Many of them had clear apical dendrite. They were likely excitatory pyramidal neurons (Fig. 1Q and R). In layers 2/3 and 4, APP_{SWE}-positive somata were rarely found in most regions (Fig. 1B–J), however in the infralimbic area, a small but substantial number of labeled somata were scattered in layers 2/3 in addition to dense labeling in layers 5 and 6 (Fig. 1B; also see Fig. 4C and D, Fig. 5H). In hippocampal formation, many positive somata were found in CA1 pyramidal layer (Fig. 1D,

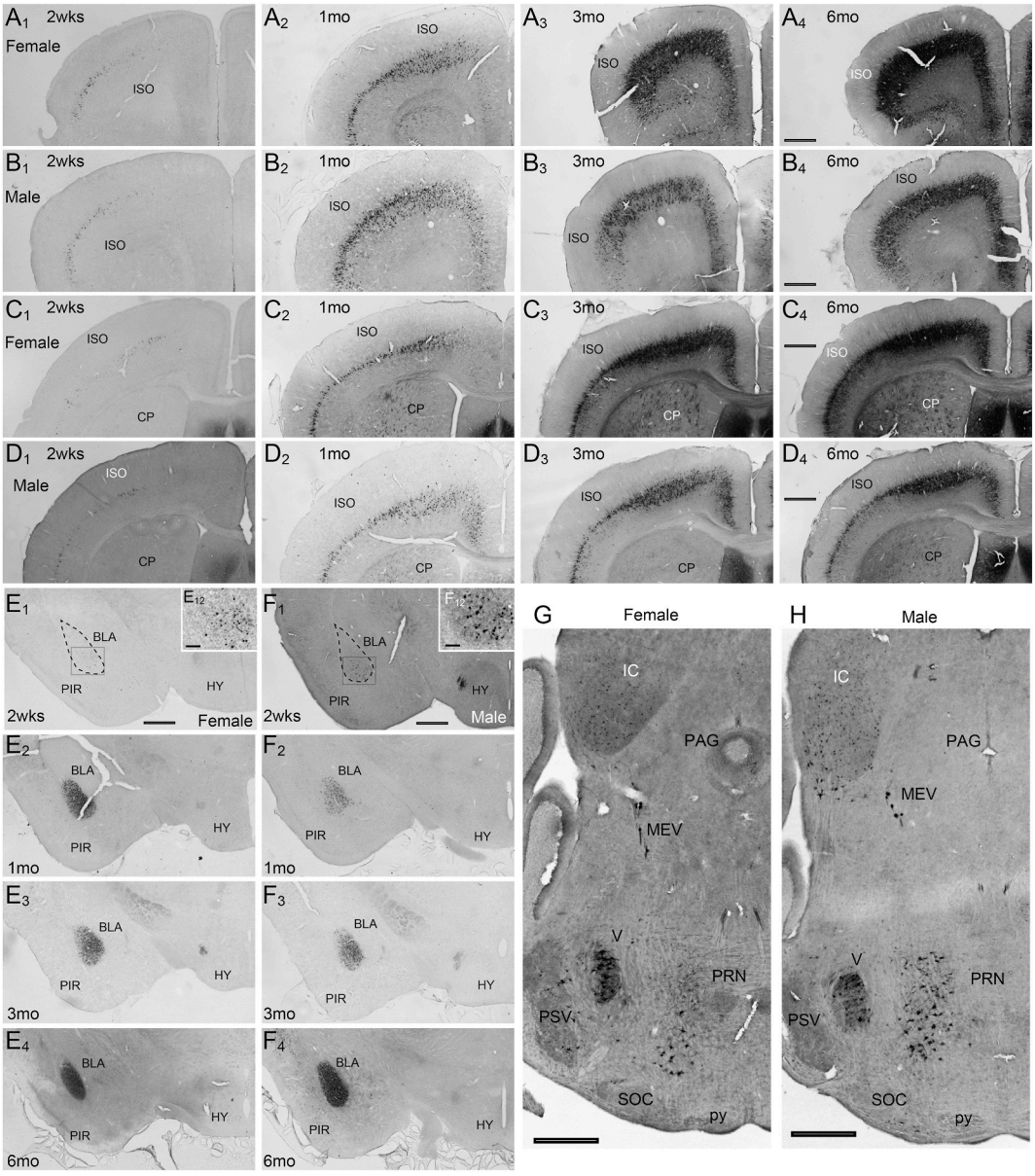

Fig. 2. Developmental changes of APP_{SWE}-positive neurons in the brain of 3xTg-AD mice. APP_{SWE} was visualized by anti-human APP antibody 1D1. The letters 2wks, 1mo, 3mo, and 6mo in each panel indicate the age of the animals at two weeks, one month, three months, and six months, respectively. Scale bar: 500 μm. (A, B) The isocortex from 2.145 mm to 1.42 mm from bregma. (A) Female. (B) Male. (C, D) The isocortex from 0.746 mm to 0.345 mm from bregma. (C) Female. (D) Male. (E, F) basolateral amygdala (BLA). The dotted line in the E_1 and F_1 indicate the border of BLA. The insets E_{12} and F_{12} show the magnified images of the areas indicated by the grey rectangles in E_1 and E_2, respectively. Scales bars in insets: 100 μm. (E) Female. (F) Male. (G, H) The images of the brainstem at 14 days of age. (G) Female. (H) Male. Abbreviations are as follows: V, motor nucleus of trigeminal; BLA, basolateral amygdala; CP, caudoputamen; HY, hypothalamus; IC, inferior colliculus; ISO, isocortex; MEV, midbrain trigeminal nucleus; PAG, periaqueductal grey; PIR, piriform area; PSV, principal sensory nucleus of trigeminal; py, pyramid; SOC, superior olivary complex.

F–I), CA3 pyramidal layer (Fig. 1D, G-I), subiculum (Fig. 1H–J), and entorhinal cortex (Fig. 1I and J). Among them, CA1 pyramidal layer was a region where APP_{SWE}-positive somata were most densely packed in the CNS (Fig. 1S). In CA3 pyramidal layer, large somata with thick dendrites were APP_{SWE}-positive (Fig. 1T). In contrast to CA1 and CA3, only a few somata were positive in CA2 (Fig. 1D–F, G). Among the subicular complex, although the neuropil stain was massive, labeled somata were only found in the subiculum (Fig. 1H–J), not in para-, post-, and pre-subiculum (Fig. 1J). In the entorhinal cortex, APP_{SWE}-positive somata were found both in the lateral and medial regions (Fig. 1I and J). The lateral entorhinal cortex (ENTl) had a unique distribution of APP_{SWE}-positive somata through the anteroposterior axis. In ENTl, more positive somata were found in layers 2/3 and 4 in anterior regions (Fig. 1I) than in posterior regions (Fig. 1J; also see Fig. 3I).

3.2. Olfactory areas

In the olfactory areas, a large number of labeled somata was found in the anterior olfactory nucleus (Fig. 1B), taenia tecta, dorsal peduncular area, and cortical amygdala area (Fig. 1E). In the olfactory bulb, labeled cell body was virtually absent (Fig. 1A). In the piriform cortex, labeled somata were primarily distributed in layer 3 (Fig. 1B–D, E).

3.3. Cortical subplate, striatum, and pallidum

Among the cortical subplate regions, the basolateral amygdala was the region with the densest distribution of labeled somata (Fig. 1D). In other amygdalar nuclei, somata were moderately or weakly stained (Fig. 1D). In addition to amygdalar structure, labeled somata were consistently found in the claustrum and endopiriform nucleus (Fig. 1E). In other regions of striatum and pallidum, only medial septal nucleus (Fig. 1C, also see Supplementary Figs. 2A and B), substantia innominata (Fig. 1E, also see Supplementary Figs. 2C and D), and bed nucleus of stria terminals (Supplementary Fig. 2C) contained a small number of positive neuronal cell bodies.

3.4. Diencephalon

In the thalamus and hypothalamus, virtually no APP_{SWE}-positive somata were found (Fig. 1F–I, K) other than in the lateral preoptic area, which had a small number of positive cell bodies.

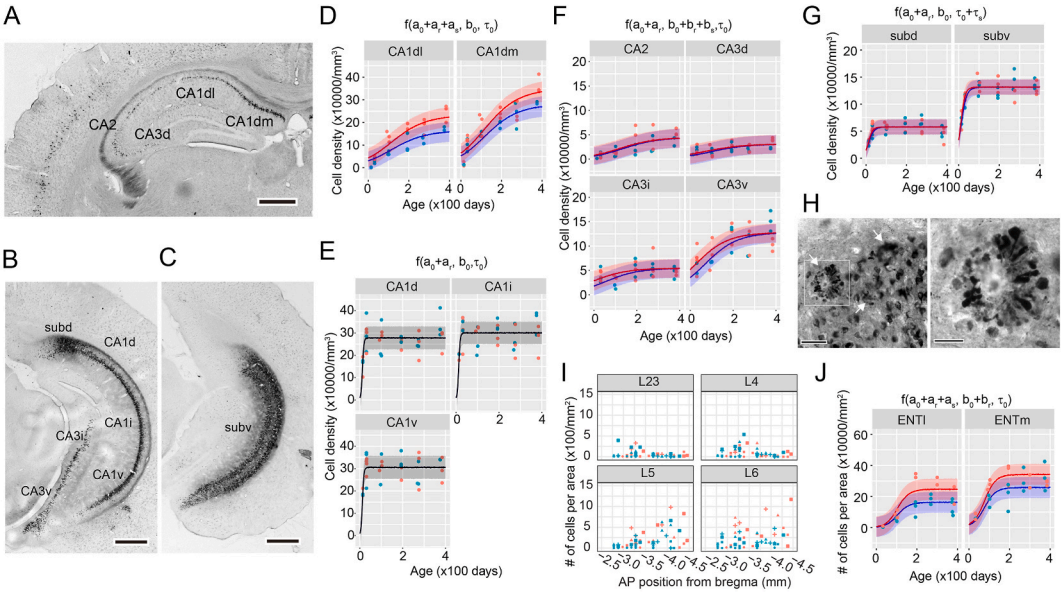

Fig. 3. The accumulation of the APP_{SWE} in the hippocampal formation. (A–C) The subdivisions of the hippocampus. The sections were obtained from a one-month-old female 3xTg-AD mouse. (A) The anterior part of the hippocampus (−2.055 mm from bregma). (B) Posterior part of the hippocampus (−3.18 mm from bregma). (C) Posterior subiculum (−3.98 mm from bregma). Scale bar: 500 μm. (D–G) The density of APP_{SWE}-positive somata was plotted against age. The logistic growth curve model fitted the data. Above the panels, we indicated the parameters used in the model of each figure. (D) Anterior CA1 regions. (E) Posterior CA1 regions. (F) CA2 and CA3 regions. (G) Subiculum regions. (H) The image of dystrophic neurites in the subiculum of a 12-month-old female 3xTg-AD mouse. The white arrows indicate dystrophic neurites. APP_{SWE} was visualized by an anti-human APP antibody 1D1. Scale bar: 50 μm. (I) The number of APP_{SWE}-positive somata per area in the lateral entorhinal cortex was plotted against the anterior-posterior position from the bregma. (J) The number of APP_{SWE}-positive somata per area in the lateral (ENTl) and medial (ENTm) entorhinal cortices was plotted against age. The logistic growth curve model fitted the data. Above the panels, we indicated the parameters used in the model.

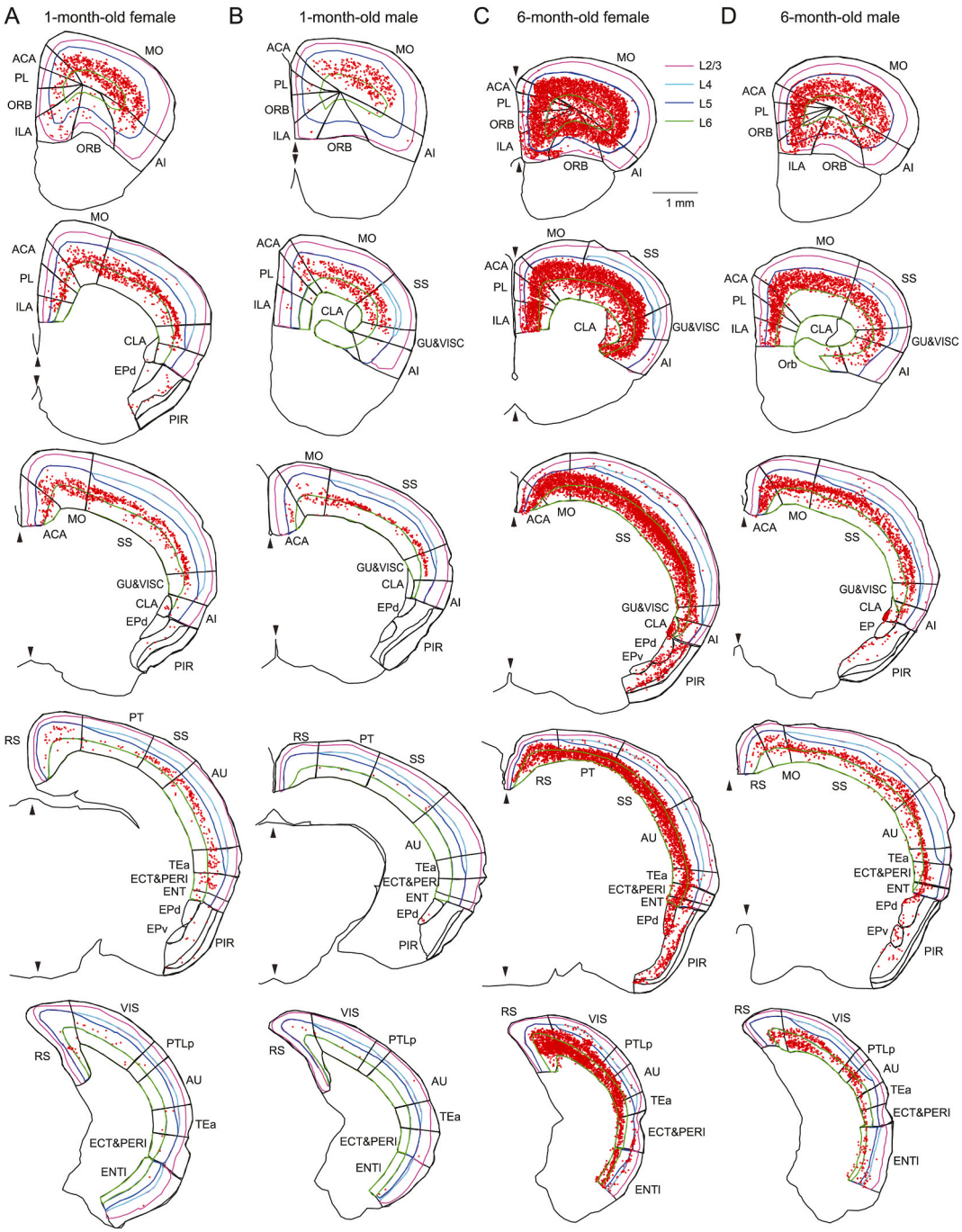

Fig. 4. The distribution of the APP_{SWE}-positive somata in the isocortex of 3xTg-AD mice. Red dots indicate the APP_{SWE}-positive neuronal somata. (A) one-month-old female. (B) one-month-old male. (C) 6-month-old female. (D) 6-month-old male. Abbreviations are as follows: ACA, anterior cingulate area; AI, agranular insular area; AUD, auditory area; ECT, ectorhinal area; GU, gustatory area; ILA, infralimbic area; MO, motor area; ORB, orbital area; PERI, perirhinal area; PL, prelimbic area; PTLp, posterior parietal area; RSP, retrosplenial area; SS, somatosensory area; TEa, temporal association area; VIS, visual area; VISC, visceral area. (For interpretation of the references to color in this figure legend, the reader is referred to the Web version of this article.)

3.5. Brainstem

In the brainstem, APP_{SWE}-positive neuronal cell bodies were found in various nuclei with different densities (Table 1). In general, labeled cell bodies were large in size and sparsely distributed in brainstem nuclei. Intriguingly, in the brainstem, labeled cell bodies

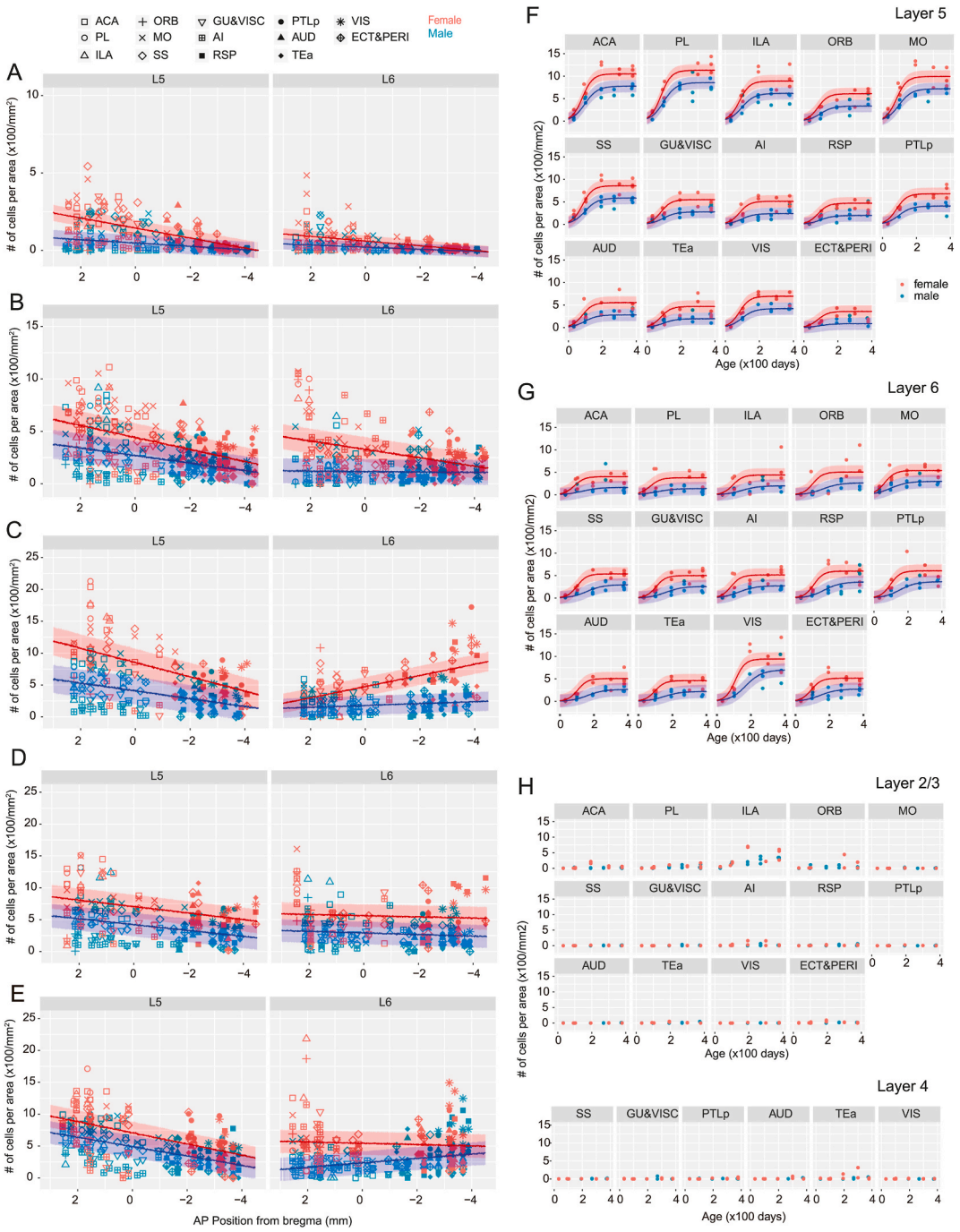

Fig. 5. The development of the somatic accumulation of APP_{SWE} in the isocortex somata. (A–E) the number of APP_{SWE}-positive somata per area in the different isocortex regions was plotted against the anterior-posterior position. The Left and right panels indicate the data of layers 5 and 6, respectively. Different symbols indicate the data of different isocortex regions. (A) One month of age. Layer 5, female, y = 144.4x + 32.3; male, y = 47.8 x + 10.7; layer 6, female, y = 60.5 + 15.3x; male, y = 21.5 + 6.9x. (B) Three months of age. Layer 5, female, y = 442.4 + 57.1x; male, y = 269.5 + 35.8x; layer 6, female, y = 328.2 + 40.0x; male, y = 116.7 + 1.99x (C) 6 months of age. Layer 5, female, y = 852.5 + 111.7x; male, y = 408.2 + 61.4x; layer 6, female, y = 474.9 -87.5x; male, y = 178.7 x −14.7x. (D) Nine months of age. Layer 5, female, y = 705.2 + 51.0x; male, y = 442.4 + 46.1x; layer 6, female, y = 562.7 + 9.3x; male, y = 291.7 x + 12.4x. (E) Twelve months of age. Layer 5, female, y = 707.3 + 87.6x; male, y = 490.6 + 73.3x; layer 6, female, y = 543.7 + 10.3x; male, y = 235.8 x – 34.6x. (F–I) The number of APP_{SWE}-positive somata per area was plotted against age. (F) Layer 5. (G) Layer 6. (H) Layer 2/3. (I) Layer 4. Abbreviations are as follows: ACA, anterior cingulate area; AI, agranular insular area; AUD, auditory area; ECT, ectorhinal area; GU, gustatory area; ILA, infralimbic area; MO, motor area; ORB, orbital area; PERI, perirhinal area; PL, prelimbic area; PTLp, posterior parietal area; RSP, retrosplenial area; SS, somatosensory area; TEa, temporal association area; VIS, visual area; VISC, visceral area.

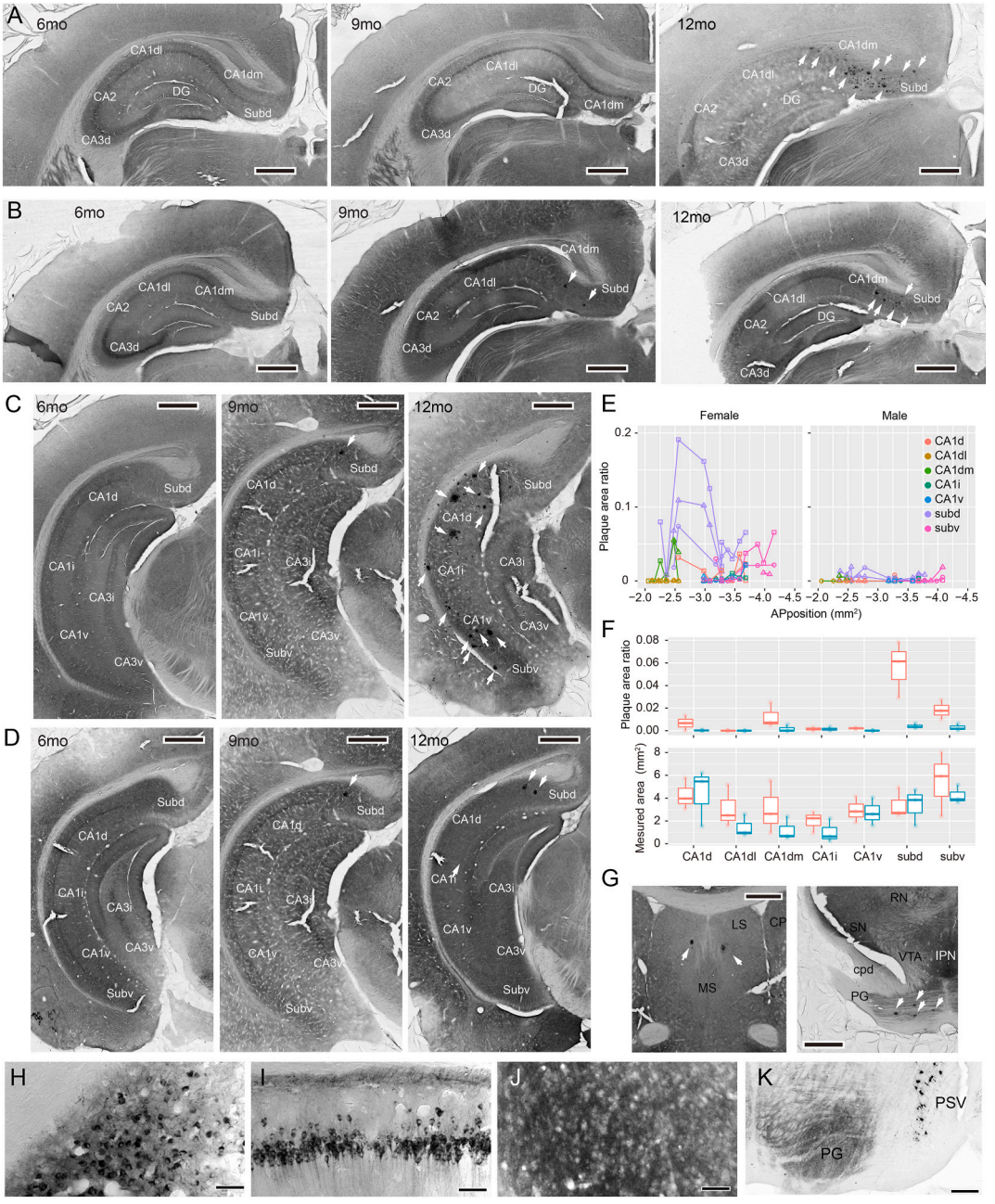

Fig. 6. The formation of amyloid plaques in the brain of 3xTg-AD mice. (A–D) immunoreactivity for β-amyloid 1-42 antibody in the hippocampus of 3xTg-AD mice. The sections from 6-month-old (left), 9-month-old (middle), and 12-month-old (right) animals are shown. (A, B) The anterior part of the hippocampus. (A) Female. (B) Male. (C, D) Posterior part of the hippocampus. (C) Female. (D) Male. Scale bar: 500 μm. The arrows indicate the clear plaque structures. Notice that the small plaques were scattered in addition to the indicated plaques in the sections from 12-month-old females. (E) Fluorescent IHC for APP_{SWE} (left) and β-amyloid 1-42 (middle) in the subiculum. The arrows in the merged image (right) indicate that dystrophic neurites surround the amyloid plaques. Scale bar: 50 μm. (E) The occupancy of amyloid plaques in different regions in CA1 and subiculum of 12-month-old females (N = 3, upper panel) and males (N = 3, lower panel) was measured and plotted. X-axis indicates the rostrocaudal position. Different colors indicate different regions in CA1 and subiculum. Different symbols indicate different animals. (F) The occupancy of amyloid plaques (upper panel) and measured area (lower panel) in different regions in CA1 and subiculum was presented in the boxplots. (G) As well as the hippocampus, amyloid plaques were frequently observed in the lateral septal nucleus (left panel) and pontine grey (right panel) in 12-month-old female 3xTg-AD mice. The arrows indicate the amyloid plaques. Scale bar: 500 μm. (H–K) The APP_{SWE}-positive somata were found in the hippocampus, not in the lateral septal nucleus and pontine grey. (H) Subiculum. (I) Dorsal CA1. (J) Lateral septal nucleus. (K) Pontine grey. All the images were obtained from female mice at nine months of age. (H–J) Scale bar: 50 μm. (K) Scale bar: 200 μm. (For interpretation of the references to color in this figure legend, the reader is referred to the Web version of this article.)

were frequently observed in the motor-related area, such as the red nucleus (Fig. 1K), the motor nucleus of the trigeminal nerve (Fig. 1L and M), oculomotor and trochlear nuclei (data not shown), the intermediate grey layer of the superior colliculus (Fig. 1H), vestibular nuclei (Fig. 1N and O). In addition, labeled cell bodies were found in the auditory nuclei (inferior colliculus, Fig. 1M; nuclei of lateral lemniscus, data not shown; superior olivary complex, Fig. 1L) other than cochlear nucleus (Fig. 1N), in midbrain trigeminal nuclei (Fig. 1M) and reticular nuclei in the midbrain, pons, and medulla (Fig. 1K-P).

3.6. Cerebellar region

In the cerebellar cortex, virtually no APP_{SWE}-positive somata were found (Fig. 1N), while positive cell bodies were found in all the deep cerebellar nuclei (Fig. 1N).

In these regions, APP_{SWE}-positive somata were observed in both males and females from 14 days of age (Fig. 2A_1, B_1, C_1, D_1, E_1, F_1, G, H). However, in the brainstem, many APP_{SWE}-positive somata were observed from this period (Fig. 2G and H), whereas sparser somata were stained in the forebrain region at 14 days of age (Fig. 2A_1, B_1, C_1, D_1, E_1, F_1). In the forebrain, the substantial number of APP_{SWE}-positive somata were observed at one month of age (Fig. 2A_2, B_2, C_2, D_2, E_2, F_2) and their number increased over the course of development (3 months of age, Fig. 2A_3, B_3, C_3, D_3, E_3, F_3; 6 months of age, Fig. 2A_4, B_4, C_4, D_4, E_4, F_4).

3.7. Antibodies for human APP1D1 and β-amyloid 6E10 showed virtually identical somatic staining patterns

In addition to anti-human APP antibody 1D1, we also examined the anti-β-amyloid 6E10 antibody, another commonly used antibody to detect human APP [6,12]. We found that the antibodies for human APP 1D1 (Fig. 1) and β-amyloid 6E10 (Supplementary Fig. 3) visualized neuronal cell bodies in virtually identical regions in the CNS. On the other hand, the antibodies for β-amyloid 1-40 and 1-42 showed much less clear somatic staining (Supplementary Figs. 1E and F) than those mentioned above (Supplementary Figs. 1C and D). Fluorescent double immunohistochemistry by anti-human APP antibody 1D1 and anti- β-amyloid 6E10 antibody revealed that most β-amyloid 6E10-positive somata were also positive for human APP 1D1 in the isocortex and CA1 (Fig. 1U, **V**, isocortex, 97.7%, APP $1D1^+/6E10^+ = 1712/1752$; CA1, 98.8%, APP $1D1^+/6E10^+ = 752/761$). The human APP 1D1-positive somata were also mostly positive for β-amyloid 6E10 (isocortex, 99.3%, $6E10^+$/APP $1D1^+ = 1712/1723$; CA1, 100%, $6E10^+$/APP $1D1^+ = 752/752$). These results suggested that both antibodies could be almost identically used to detect APP_{SWE}-positive somata. Thus, in the subsequent quantitative analysis, we used the data from human APP 1D1 and β-amyloid 6E10 IHC for the hippocampus and isocortex, respectively. In the hippocampus, human APP IHC had lower intercellular staining than β-amyloid 6E10 IHC because it did not bind to β-amyloid (Fig. 3A–C, Supplementary Fig. 3F-I), which seemed to be rich around the pyramidal layer of cornu ammonis (see Supplementary Figs. 1E and F). In the isocortex, somata were more visible in β-amyloid 6E10 IHC than in human APP IHC because dendrites and fibers were more intensely stained in human APP1D1 IHC (Fig. 1B–J) than in β-amyloid 6E10 IHC (Supplementary Figs. 3B–I).

3.8. Developmental increase of the number of APP_{SWE}-positive somata in the hippocampus

To examine how the APP_{SWE}-positive somata increased with development in the hippocampus, we measured the density of somata visualized by human APP1D1 IHC with the optical dissector stereological method (see **Materials and Methods**). In the hippocampus, there was a region-specific difference in the density of APP_{SWE}-positive somata: The density of APP_{SWE}-positive somata was much higher in CA1 than in CA2 and CA3 (Fig. 3A–F). Further, in the CA1, the posterior CA1 had an earlier developmental increase of APP_{SWE}-positive somata than the anterior CA1 (Fig. 3A, B, D, E). In the anterior CA1, the medial region had more APP_{SWE}-positive somata than the lateral region (Fig. 3A–D). Considering these region-dependent differences, we examined the developmental increase of somatic APP_{SWE} accumulation in the CA1 (Fig. 3D and E) by measuring the density of APP_{SWE}-positive somata in different regions. Following the previous studies on CA1 subdivision [13,14], we separated the CA1 into six regions (Fig. 3A, B, D, E): anterior

Table 2
The number of the animals used for the number of APP_{SWE}-positive somata in the hippocampus[a].

	2-weeks-old	1-month-old	3-month-old	6-month-old	9-month-old	12-month-old	Total
CA1dm	(2, 2)	(4, 3)	(3, 3)	(3, 3)	(3, 3)	(3, 2)	(18, 16)
CA1dl	(2, 2)	(4, 3)	(3, 3)	(3, 3)	(3, 3)	(3, 2)	(18, 16)
CA1d	(2, 2)	(4, 3)	(3, 3)	(3, 3)	(3, 3)	(3, 3)	(18, 17)
CA1i	(2, 2)	(4, 3)	(3, 3)	(3, 3)	(3, 3)	(3, 3)	(18, 17)
CA1v	(2, 2)	(4, 3)	(3, 3)	(3, 3)	(3, 3)	(3, 3)	(18, 17)
CA2	(0, 1)	(4, 3)	(3, 3)	(3, 3)	(3, 3)	(3, 2)	(16, 15)
CA3d	(0, 1)	(4, 3)	(3, 3)	(3, 3)	(3, 3)	(3, 2)	(16, 15)
CA3i	(0, 0)	(4, 3)	(3, 3)	(3, 3)	(3, 3)	(3, 3)	(16, 15)
subd	(2, 2)	(4, 3)	(3, 3)	(3, 3)	(3, 3)	(3, 3)	(18, 17)
subv	(2, 2)	(4, 3)	(3, 3)	(3, 3)	(3, 3)	(3, 3)	(18, 17)
ENTl	(0, 0)	(2, 2)	(3, 3)	(2, 3)	(2, 3)	(2, 4)	(11, 15)
ENTm	(0, 0)	(3, 1)	(3, 3)	(3, 3)	(2, 3)	(3, 3)	(14, 13)

[a] The number of animals used is presented as (Nf, Nm) for the different ages, where Nf is the number of females and Nm is the number of males, respectively.

mediodorsal CA1 (CA1dm), anterior laterodorsal CA1 (CA1dl), posterodorsal CA1 (CA1d), posterior intermediate CA1 (CA1i), and posteroventral CA1 (CA1v). The number of animals used for this analysis is presented in Table 2. The developmental changes of APP_{SWE}-positive somata in these regions were well-fitted by the logistic growth curve model (Fig. 3D and E). To choose the best model, we assessed the models with and without region- and sex-effects for a, b, and τ by Widely Applicable Information Criterion (WAIC) and chose the model with the least WAIC among tested models. For assessing the models, we first tested the models with the region-effects. After choosing the best model with region effects, we examined the sex effects on the model and finally chose the best composite Model (Supplementary Fig. 4). The modeling showed that the developmental increase of APP_{SWE}-positive somata was much faster in the posterior CA1 regions (Fig. 3E, $\tau_0 = 3.5$) than in the anterior CA1 regions (Fig. 3D, $\tau_0 = 81.7$). In the anterior CA1 regions, the cell density of APP_{SWE}-positive somata was higher in females than in males (Fig. 3D, female, $a_s = 33721.2$; male, $a_s = -33962.7$), while there was no sex-dependent difference in the posterior regions but only region-dependent (CA1d, $a_r = -16522.1$, CA1i, $a_r = 6095.92$, CA1v, $a_r = 11260.8$). Further, we measured the density of APP_{SWE}-positive somata in the CA2-3 (Fig. 3F). As well as CA1, CA3 was separated into dorsal CA3 (CA3d), intermediate CA3 (CA3i), and ventral CA3 (CA3v) [14]. In CA2-3, the APP_{SWE} cell density was much lower than in CA1, except ventral CA3 (Fig. 3F, anterior CA1, $a_0 = 256546.8$; posterior CA1, $a_0 = 294428.0$; CA2-3, $a_0 = 66309.8$), and its developmental increase was slower ($\tau_0 = 75.5$) than in posterior CA1. In addition to cornu ammonis, we measured the developmental changes of APP_{SWE}-positive somata in the subiculum (Fig. 3G). For the subiculum, the anterodorsal (subd) and posteroventral (subv) regions were separately evaluated (Fig. 3B, C, G). In the subiculum, APP_{SWE}-positive somata were sparser than in CA1 pyramidal layers (subd, $a_0 + a_r = 57785.8$; subv, $a_0 + a_r = 131535.4$). The developmental increase of APP_{SWE}-positive somata started at an early age (Fig. 3G; $\tau 0 = 18.6$), and it was slightly faster in females ($\tau 0 + \tau s = 10.9$) than in males($\tau_0 + \tau_s = 13.9$). In the subiculum and CA1 of the female mice of 9 and 12 months, swollen neuronal processes were occasionally observed by APP 1D1 staining (Fig. 3H). These structures were often radially arranged to the center of the blank (Fig. 3H) and were considered dystrophic neurites in the peripheral zone of amyloid plaques [15,16], which was previously shown immunoreactive for APP [17].

In addition to these hippocampal regions, we examined the development of APP_{SWE}-positive somata in the entorhinal cortex, the primary gateway between the hippocampus and isocortex, which is known to have pathological symptoms at an early stage of AD in humans [18]. As mentioned above, in the lateral entorhinal cortex (ENTl), more APP_{SWE}-positive somata were distributed in layers 2/3 and 4 in the anterior areas than in the posterior areas (Fig. 3I). By measuring the number of APP_{SWE}-positive somata per area by using Neurolucida software, the increase of APP_{SWE}-positive somata was examined in ENTl, and medial entorhinal cortex (ENTm, Fig. 3J). Compared with posterior CA1 and subiculum, the increase of APP_{SWE}-positive somata was slower in the entorhinal cortices ($\tau_0 = 27.3$). The amount of APP_{SWE}-positive somata was more abundant in the ENTm ($a_0 + a_r = 280.5$) than in the ENTl ($a_0 + a_r = 375.9$). In the entorhinal cortices, females had more APP_{SWE}-positive somata (Fig. 3J, $a_s = -33.5$) than males ($a_s = -118.0$).

3.9. Developmental changes in the number of APP_{SWE}-positive somata in the isocortex

Next, to evaluate the number of APP_{SWE}-positive somata in the different isocortex regions, we counted the somata visualized by β-amyloid 6E10 IHCwith Neurolucida software (Fig. 4, the number of animals measured for each region is shown in Table 3). In the isocortex, APP_{SWE}-positive somata developmentally increased (Figs. 4, 5F, G) with the region-dependent difference: The number of APP_{SWE}-positive somata per area was higher in anterior regions than in posterior regions (Fig. 5A–E), which was apparent in particular at one month of age (Fig. 4A and B). In layer 5, this trend was observed at all the examined ages (Fig. 5A–E), while in layer 6, the regional difference disappeared as the age increased (Fig. 5A–E). In addition to regional differences, the number of APP_{SWE}-positive somata per area in the isocortex also had sex-dependent differences: it was higher in females than in males (Figs. 4, 5). In Fig. 5F–H, we plotted the number of APP_{SWE}-positive somata per area against age. In layers 5 (Figs. 5F) and 6 (Fig. 5G), APP_{SWE}-positive somata developmentally increased in all the isocortex regions. In contrast, layers 2-3 (Fig. 5H, upper panels) and 4 (Fig. 5H, lower panels) had only a small number of APP_{SWE}-positive somata in all the ages, except layer2-3 of ILA (Fig. 5H, upper panels). The logistic growth curve

Table 3
The number of the animals used for the number of APP_{SWE}-positive somata in the isocortex[a].

	1-month-old	3-month-old	6-month-old	9-month-old	12-month-old	Total
ACA	(2, 3)	(3, 3)	(2, 3)	(2, 3)	(3, 4)	(12, 16)
AI	(2, 3)	(3, 3)	(2, 3)	(2, 3)	(3, 4)	(12, 16)
AUD	(2, 3)	(3, 3)	(2, 2)	(2, 3)	(3, 4)	(12, 15)
ECT&PERI	(2, 3)	(3, 3)	(2, 3)	(2, 3)	(3, 4)	(12, 16)
GU&VISC	(2, 3)	(3, 3)	(2, 3)	(2, 3)	(3, 4)	(12, 16)
ILA	(2, 3)	(3, 3)	(2, 3)	(1, 3)	(3, 3)	(11, 15)
MO	(2, 3)	(3, 3)	(2, 3)	(2, 3)	(3, 4)	(12, 16)
ORB	(2, 3)	(2, 3)	(1, 2)	(2, 3)	(2, 3)	(9, 14)
PL	(2, 3)	(3, 3)	(1, 3)	(2, 3)	(3, 4)	(11, 16)
PTLp	(2, 2)	(3, 3)	(1, 2)	(2, 3)	(3, 4)	(11, 14)
RSP	(2, 3)	(3, 3)	(2, 3)	(2, 3)	(3, 4)	(12, 16)
SS	(2, 3)	(3, 3)	(2, 3)	(2, 3)	(3, 4)	(12, 16)
TEa	(2, 3)	(3, 3)	(2, 3)	(2, 3)	(3, 4)	(12, 16)
VIS	(2, 2)	(2, 3)	(1, 2)	(2, 3)	(2, 4)	(11, 12)

[a] The number of animals used is presented as (Nf, Nm) for the different ages, where Nf is the number of females and Nm is the number of males, respectively.

model fitted the data of layers 5 and 6, showing the developmental increase of APP_{SWE}-positive somata had region- and sex-dependencies. All the values of the parameters in the models were in Supplementary Table 1 (layer 5) and **2** (layer 6). The region effect was on the number of positive somata (a) in layer 5 (Fig. 5F–Supplementary Table 1), whereas it was on the initial value of positive somata (b) as well as a in layer 6 (Fig. 5H–Supplementary Table 2). On the other hand, the sex effect was on a and the time constant (τ) in both layers 5 and 6 (Fig. 5F and G): females (layer 5, $a_s = 105.1$; layer 6, $a_s = 83.1$) had more positive somata than males (layer 5, $a_s = -168.2$; layer 6, $a_s = -157.7$), and the increase of positive somata was faster in female (layer5, $\tau_s = -2.8$; layer 6, $\tau_s = -9.1$) than in males (layer5, $\tau_s = 3.4$; layer 6, $\tau_s = 7.6$). Compared with the hippocampus, the isocortex had less numerous positive somata (layer 5, $a_0 = 597.5$; layer 6, $a_0 = 446.5$; note that these values were the number of somata per mm^2 in 40 μm sections, thus multiply by 25 to obtain the approximate value of mm^3 density.) and slower increase of positive somata (layer 5, $\tau_0 = 33.4$; layer 6, $\tau_0 = 37.6$) than posterior CA1 and subiculum. Further, these results suggested that the isocortex and entorhinal cortex in 3xTg-AD mice had similar development of APP_{SWE}-positive somata.

3.10. *Amyloid plaques were primarily formed in the hippocampus in the brain of 3xTg-AD mice*

Finally, we examined how amyloid plaques formed developmentally in the brains of 3xTg-AD mice. Following the previous studies [9,19], the amyloid plaques were visualized by β-amyloid 1-42 IHC (see **Materials and Methods**). We stained the sections from the animals of three months, six months (Fig. 6A–D, left panels), nine months (Fig. 6A–D, middle panels), and twelve months (Fig. 6A–D, right panels) of age (for each age, female = 3, male = 3). We found that amyloid plaques first formed in the subiculum and CA1 at around nine months of age (Fig. 6A–D). We could not find extracellular-amyloid plaques in the sections from females and males of three months (data not shown) and six months of age (Fig. 6A–D, left panels). To rule out the possibility that β-amyloid 1-40 formed the β-amyloid plaques earlier, we performed β-amyloid 1-40 IHC for the sections from 6-month-old females (N = 5) and found no plaques in any brain areas (data not shown).

The plaques were frequently found in 9- and 12-month-old animals at the border between the subd and CA1d (Fig. 6A and B). At 12 months of age, more plaques were found in the subiculum and CA1 than at nine months (Fig. 6A–D). To quantitatively evaluate the amount of amyloid plaque, we measured the area of amyloid plaques using ImageJ (**Material and Method**). In Fig. 6E, the ratio of amyloid plaque area to measurement area in each brain section was plotted against the anterior-posterior position of the measured section. It showed that female mice (N = 3) had more plaques than males (N = 3), forming primarily in the subiculum. To statistically compare the regional- and sex differences in plaque formation, we calculated the ratio of amyloid plaque area to the total measured area in each region (Fig. 6F, upper panel). Two-way ANOVA indicated that the plaques formed differently by sex ($F(1,28) = 25.3$, $P = 2.55 \times 10^{-5}$) and region ($F(6,28) = 10.6$, $P = 3.81 \times 10^{-6}$). These differences were unlikely due to the measurement bias because each region was fully investigated in females and males (Fig. 6F, lower panel; two-way ANOVA, sex, $F(1,28) = 2.6$, $P = 0.115$, region, $F(6,28) = 3.4$, $P = 0.0128$). In addition to these regions, some plaques were found in the lateral entorhinal cortex of 12-month-old females (N = 3). In contrast to the hippocampus, up to 12 months of age, we did not find clear large amyloid plaques in the isocortex, but only tiny ones if they ever existed. A similar distribution was reproduced in the plaque of β-amyloid 1-40 IHC (12-month-old

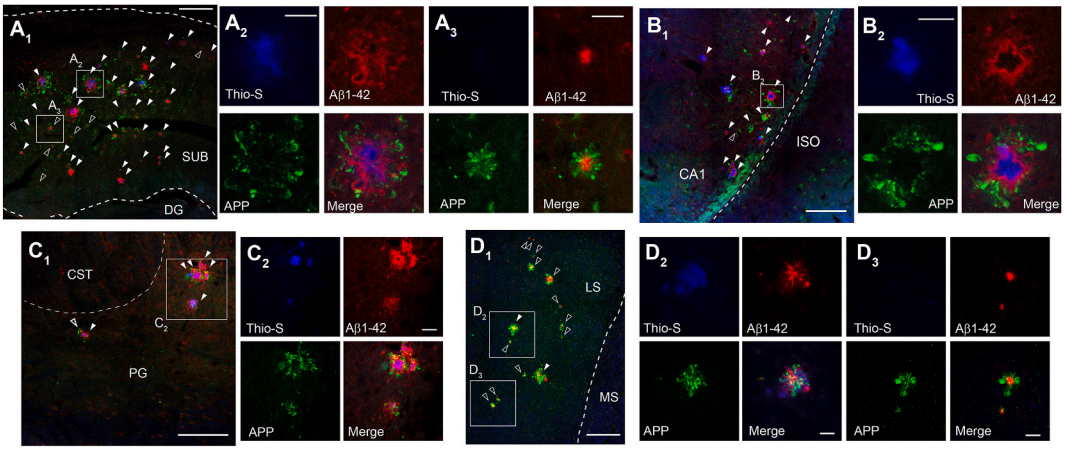

Fig. 7. Neuritic amyloid plaques in the brain of 3xTg-AD mice. (A–D) the triple fluorescent immunohistochemical images. Blue, red, and green signals are for Thioflavins-S, APP 1D1, and β-amyloid 1-42, respectively. (A) Subiculum. (B) CA1. (C) Pontine grey. (D) Lateral septal nucleus. (A_1, B_1, C_1, D_1) The tiled images were obtained with an x 40 lens using tile scanning and z-stacked over the entire thickness of the section. Filled and open arrowheads indicate Thioflavin+/β-amyloid 1-42+ plaques and Thioflavin-/β-amyloid 1-42+ plaques, respectively. Scale bars: 100 μm. (A_2, A_3, B_2, C_2, D_2, D_3) The higher-magnification images of the area are indicated by the white square in the tiled images. The higher-magnification images were obtained with x63 lenses in 3 μm increments along the z-axis, of which 2-3 were z-stacked. Scale bars: 20 μm. All the images were obtained from female mice at twelve months of age. Scale bars: left panels = 100 μm; right panels = 20 μm. Abbreviations are as follows: CST, corticospinal tract; DG, dentate gyrus; ISO, isocortex; LS, lateral septal nucleus; MS, medial septal nucleus; PG, pontine grey; SUB, subiculum. (For interpretation of the references to color in this figure legend, the reader is referred to the Web version of this article.)

females, N = 2, data not shown): plaque was seen mainly in the subiculum and CA1 but hardly in the isocortex. In addition to the hippocampus, the amyloid plaques were frequently found in the lateral septal nucleus (Fig. 6G, left panel) and pontine grey (Fig. 6G, right panel) in the brain of female 3xTg-AD mice at 12 months of age (N = 3). In 12-month-old males, we did not find plaques in these regions (N = 3). Unlike the subiculum (Fig. 6H) and CA1 (Fig. 6I), these areas contained only APP_{SWE}-positive fibers without APP_{SWE}-positive somata (pontine grey, Fig. 6J; lateral septal nucleus, Fig. 6K). These results suggested that the β-amyloid could be released from the axonal fibers [20].

Furthermore, we examined if the plaques in the brain of 3xTg-AD mice were neuritic: A neuritic plaque has surrounding dystrophic neurites and often a dense amyloid core [16]. We used Thioflavin-S to visualize the dense amyloid core, which strongly binds the fibrillogenic amyloid core [16]. For dystrophic neurites, which were reported immunopositive for APP [15,17], we used anti-human APP antibody 1D1 that stained abnormally swollen neuronal processes in bright-field IHC (Fig. 3H). The triple fluorescent staining for β-amyloid 1-42, APP1D1, and Thioflavin-S showed that many plaques in the brain of 3xTg-AD mice (12-month-old females) were neuritic, having surrounding APP1D1-positive dystrophic neurites and Thioflavin-positive core (Fig. 7). We found the neuritic plaques with a Thioflavin-positive core (Thio-S^+ neuritic plaques) in the subiculum (Fig. 7A_1, A_2), CA1 (Fig. 7B_1, B_2), pontine grey (Fig. 7C_1, C_2), and lateral septal nucleus (Fig. 7D_1, D_2). In addition to the neuritic plaques with a Thioflavin-positive core, we found some without a Thioflavin-positive core (Thio-S^- neuritic plaques; Fig. 7 A_1, A_3, D_1, D_3). These plaques had surrounding dystrophic neurites but were negative for Thioflavin (Fig. 7A_3, D_3) and had relatively small β-amyloid staining areas (<10 μm diameter). To examine the proportion of Thio-S^+ and Thio-S^- neuritic plaques in the subiculum, CA1, pontine grey, and lateral septal nucleus, we count them in each region in two sections from 12-month-old 3xTg-AD females (N = 2). We found both Thio-S^+ and Thio-S^- neuritic plaques in all these regions. In subiculum, CA1 and pontine grey, the Thio-S^+ plaques were a majority (subiculum, ThioS^+:Thio-S^- = 53:10; CA1, ThioS^+:Thio-S^- = 30:5; pontine grey, ThioS^+:Thio-S^- = 31:6), whereas the lateral septal nucleus had more Thioflavin-negative plaques (ThioS^+:Thio-S^- = 4:20; Fig. 7D_1). These results suggested that the amyloid plaques in the 3xTg-AD mice were mostly neuritic.

4. Discussion

In this study, we elucidated that the development of somatic accumulation of APP_{SWE} was different in the brain regions and sex of 3xTg-AD mice. We found that APP_{SWE}-positive somata were broadly distributed in the brain of 3xTg-AD mice (Fig. 1). In addition to the isocortex and hippocampus, many APP_{SWE}-positive somata were found in the olfactory areas, amygdala, and many nuclei in the brainstem (Fig. 1) from the early developmental stage as two weeks of age (Fig. 2A_1, B_1, C_1, D_1, E_1, F_1, G, H), which is consistent with Thy1-driven transgene expression patterns in some transgenic mice [21,22]. Also, this is consistent with the previous studies that examined the distribution pattern of 6E10 positive neurons in the brain of 3xTg-AD mice [7,8]. These results suggested that the 3xTg-AD mice might have some behavioral and psychological abnormalities related to the function of these brain areas because the excessive accumulation of APP could alter the neuronal activities via their effects on the ion channels [23]. It is well known that AD symptoms include disturbances in mood, emotion, motor function, and others [24,25], which could be relevant to the disorders in the subcortical area [24]. Although most previous studies on 3xTg-AD mice have been focused on cognitive deficits, it might be worthwhile to scrutinize emotional or motor functional symptoms more closely in this AD model.

This study used anti-human APP antibody 1D1 and anti-β-amyloid 6E10 antibody to detect the APP_{SWE}-positive somata. IHC confirmed that the neuronal population stained by these antibodies was nearly identical in the isocortex and hippocampus (Fig. 1U and V). This result was unexpected because anti-β-amyloid 6E10 antibody binds to the C-terminal fragments of APP and β-amyloid as well as full-length APP (see Material and Method); however, most β-amyloid 6E10 positive neurons were also positive for human APP1D1 (see Results). As for β-amyloid, the anti-amyloid-6E10 antibody binding might be limited to its monomer [26], which led to weak staining. As for C-terminal fragments, many of them might not be present on the neuronal membrane by themselves but coexist with APP. Anti-human APP antibody 1D1 stained the APP-positive dendrites (Fig. 1Q and R) and fibers (Fig. 6J and K) as well as APP-positive somata. Therefore, intense staining was seen in APP-positive fiber-rich areas such as CA1 and subiculum (Fig. 1F–J), especially when the DAB reaction time was long (15 min for the sections in Fig. 1 except G and H).

To test the relationship between somatic APP accumulation and age, we used a Bayesian model method (Fig. 3D–G, J, 5F, G). We created models with or without region and sex effects in the parameters of the logistic growth function (Materials and Methods) and estimated the best model among them based on WAIC, a good predictability index (Supplementary Fig. 4). By taking this approach, we were able not only to statistically verify whether there were differences by region or sex but also to estimate the amount and time courses of somatic APP accumulation (Fig. 3D–G, J, 5F, G), thereby providing a dynamic perspective of APP pathology that conventional statistics would not confer. In the hippocampus and isocortex, the accumulation of the somatic APP_{SWE} had regional differences: in the CA1 and subiculum, more APP_{SWE}-positive somata were found from an early age than in CA2 and CA3 (Fig. 3D–G). Further, the increase of APP_{SWE}-positive somata in posterior CA1 (Fig. 3E) and subiculum (Fig. 3G) was faster than in anterior CA1 (Fig. 3D). On the other hand, in the isocortex, more APP_{SWE}-positive somata were found earlier in the anterior regions than in the posterior regions (Figs. 4 and 5A-E), which was also seen in a previous study that used the 6E10 antibody [7]. Although it is unclear how these regional differences were formed, several factors could underlie them. First, the Thy1-driven APP_{SWE} expression might have regional gradation. It is known that transgenic lines generated from the same construct with Thy1 regulatory elements showed a remarkable diversity in the expression of the transgene [21], which is likely to be due to the variation in the transgene integration sites [21,27]. In line with this idea, the expression of mutated human tau, which is cointegrated at the same site with APP_{SWE} [6], also showed a similar rostrocaudal distribution in the hippocampus (data not shown). Second, the trafficking and metabolism of APP might be different in diverse cell types. Generally, in neurons, transgenes driven by the Thy1 promoter have been reported to show increased expression during early postnatal days [21], reflecting the time course of the natural Thy1 expression [28]. Thus, some interferences in

metabolic processing might be relevant to the slow APP_{SWE} accumulation observed in some of our results (e.g., isocortex). It has been reported that APP undergoes highly intricate cellular trafficking and metabolism, including the generation of β-amyloid [29]. Substantial APP is distributed in the axon and plays multiple physiological roles in synapses and neurites [29,30]. In AD, the disorder in axonal trafficking frequently occurs [31,32]. The soluble β-amyloid [33] and the state of tau [34] were reported to affect the axonal transport, which might lead to the excess accumulation of APP_{SWE} in the soma [35].

In addition to the regional differences, the amount of APP_{SWE}-positive somata showed sex-dependent differences in some regions: Females had more APP_{SWE}-positive somata in the isocortex (Fig. 2A–D, 4, 5A-G) and anterior CA1 (Fig. 3D). Intriguingly, this result is consistent with the higher risk of AD in women than in men in humans [36]. However, the sexual dimorphism in the 3xTg-AD mice has been controversial: the early study on this animal did not observe the sexual differences in pathology [6]; however, many subsequent works reported that the accumulation of β-amyloid was faster in females than in males (reviewed in Ref. [10]. Furthermore, a recent Western blot study on 3xTg-AD mice showed that the APP_{SWE} accumulation in the somatosensory cortex of females was greater than that of males at the age of 3 months [37]. Recently, a systematic phenotyping work from the originator's lab [38] clearly showed that amyloid plaques, soluble and insoluble β-amyloid, are more abundant in females than males and suggested that this discrepancy with the early works could be the result of genetic drift that occurred in the colonies. They also suggested that the sexual dimorphism in the 3xTg-AD mice is likely due to the Thy1 mini-gene, which contains an estrogen response element and produces greater expression in females [39].

Finally, we found that the amyloid plaques were first formed in the hippocampal formation (Fig. 6A–D). The onsets and region of the amyloid plaques also have been controversial. The early work showed that the amyloid plaques were formed in the neocortex at six months [6]. However, recent systematic work showed that it is not valid for the animals in the current colonies [38]. This is consistent with recent works on 3xTg-AD mice [7,9,40], although the onsets of the formation of plaques were somewhat varied among them (6 months, Belfiore et al., 2019: 9 months, Oh et al., 2010; Perez et al., 2011). These differences were unlikely due to differences in the antibodies used because Belfiore et al. used the same antibody as our study (anti- β-amyloid 1-42 antibody), while Oh et al. and Perez et al. used anti-β-amyloid 6E10) for plaque visualization. However, it is possible that we underestimated plaque size because we used an antibody that recognizes the full length of β-amyloid 1-42 because β-amyloids of different lengths contribute to plaque formation [3,4]. Among the subregions in the hippocampal formation, the subiculum was the most common site for amyloid plaques [7]. In line with the early somatic APP_{SWE} accumulation (Fig. 3E), more amyloid plaques were found in the posterior part of the hippocampal formation (Fig. 6A–D) [9]. These results suggested that the APP_{SWE} accumulation in the neuron was closely relevant to the formation of the amyloid plaques since posterior CA1 and subiculum were the first sites for the neuronal APP accumulation to occur in the densely packed somata from the very early ages (Fig. 3E–G). Intriguingly, outside of the CA1 and subiculum, we found that the amyloid plaques were frequently formed in the pontine grey, as reported by Overk et al., 2009, and lateral septal nucleus. These structures did not contain the APP_{swe}-positive neuronal somata, but only APP_{swe}-positive fibers, which are from the hippocampus for the lateral septal nucleus [41,42] and isocortex for pontine grey [43], respectively. These results strongly suggested that substantial β-amyloid was released from the terminals of neurons as well as dendrites [20,44]. Considering this terminal release, the frequent formation of the plaques in the subiculum could likely be fairly due to the massive afferent inputs from the CA1 region ([45], https://connectivity.brain-map.org/) where APP_{SWE} were accumulated in the densely packed somata from an early age (Fig. 2). It is important to note, however, that 3xTg-AD mice have an abnormal tau protein expression, which may affect the intracellular APP dynamics [34].

The results of our study suggested that the plaque formation is relatively slow in 3xTg-AD mice compared to other AD model mice (the onset of plaque formation, APP/PS1dE9, 4–6 mo [46,47]; 5xFAD, 2mo [47,48]; App^{NL-F}, 6 mo [49]; App^{NL-G-F}, 2 mo [49,50]). In addition, while other animal models showed plaque formation in the isocortex from the early stages [46–49], 3xTg-AD mice showed almost no plaque in the isocortex up to 12 months of age. Considering these differences would be important in choosing the appropriate AD animal model for the experiment, although it is difficult to address what causes the differences in plaque formation in these model animals because they differ in various factors: the type of APP mutation, the promoter of the mutant APP, and whether they are knock-in or transgenic. Further, sexual dimorphism was observed in plaque formation as well as in the somatic accumulation of APPswe (Fig. 6A–G) in the brain of 3xTg-AD mice. Increased β-amyloid burden in the female has been reported in several lines of AD model mice (APP/PS1dE9 [51,52], 5xFAD [53], Tg2576 [54]), including transgenic animals expressing mutant APP by promoters other than Thy1 (APP/PS1dE9, Tg2576: mouse prion protein promoter). Recent studies have shown sexual differences in microglial function and APOE4 regulation [55], which may contribute to the difference in plaque formation in females and males. However, the sexual dimorphism in the plaque formation was not seen in APP knock-in animals [50,56], in which the mutant APP is regulated by the endogenous mouse APP promoter [49]. Thus, the possibility that sexual dimorphism in transgenic animals is an artifact of the regulation of APP expression by an exogenous promoter remains to be ruled out.

Our results showed that the formation of plaques (Fig. 6A–G) occurred much later than the somatic accumulation of APP_{swe} (Fig. 2A–D, 3D-G, J, 5A-G). The formation of plaques occurred around nine months (Fig. 6B–D) around subd, whereas the increase of APPswe-positive somata in subd and posterior CA1, a source of synaptic inputs to subd, reached a plateau within 1–2 months (Fig. 3E–G). Further, the increase of APPswe-positive somata in the motor cortex reached a plateau around six months (Fig. 5F and G), whereas the formation of plaques in pontine grey, where receives massive inputs from the motor cortex [45], occurred around 12 months (Fig. 6G, right panel). These results suggest that plaque formation proceeds several months after the accumulation of APP_{swe}. Furthermore, it was also suggested that there was a close relationship between APP accumulation and plaque formation because plaques were found only at the site of significant somatic or axonal accumulation of APP_{swe}, and more plaques were formed in females. However, note that some areas with substantial APP_{swe} accumulation did not show plaque formation (e.g., AON, BLA, etc), suggesting that there are additional determinants of the susceptibility of plaque formation. In 3xTg-AD mice, deficits in learning and memory were observed around six months of age before plaque formation began [57,58]. Thus, it is suggested that the accumulation of soluble

β-amyloid and APP could affect the cognitive behavior of 3xTg-AD mice.

By triple fluorescent stainings, we found that many amyloid plaques in the brain of 3xTg-AD mice were neuritic, surrounded by APP-positive dystrophic neurites (Fig. 7). This finding is consistent with the observation of dystrophic neurite formation almost simultaneously with plaque formation in other AD model animals [47]. Further, the observation that neuritic plaques were found in the pontine grey (Fig. 7C) and lateral septal nucleus (Fig. 7D) is consistent with the findings that some dystrophic neurites are synaptic in origin [15,59,60]. Previous studies have suggested that the internalized β-amyloid at dystrophic terminals can aggregate into fibrils that extend to extracellular space and form plaques [59,61]. The idea that dystrophic neurites are the origin of the amyloid plaques is consistent with our results showing that many plaques were neuritic, even in the regions where APP_{swe}-positive neuronal somata and dendrites were absent. In neuritic plaques, two types were found, Thioflavin-positive and negative, the former being more common in the subiculum, CA1, and pontine grey, and the latter in the lateral septal nucleus. However, this difference by region was not statistically confirmed due to the small sample size ($N = 2$). Thioflavin-positive and negative plaques might correspond to dense core plaques and diffuse plaques [15,16]. Previous studies suggested that the neuritic dense core plaques were mature plaques formed by the growth of diffuse plaques [62]. The regional differences in the ratio of Thioflavin-positive and negative plaques might reflect the time course of the formation of β-amyloid depositions. Some of the dystrophic neurites in the brain of AD patients contain paired helical filaments composed of tau [15]. It remains unclear whether this type of plaque is present in the brain of 3xTg-AD mice.

In summary, we elucidated the distribution of APP_{SWE}-positive somata in the brain and the time courses of the increase of somatic APP_{SWE} accumulation in the hippocampus, isocortex, and other regions. Our results suggested that the APP_{SWE} accumulation in the neurons was closely connected to the formation of the β-amyloid plaques, and β-amyloid was likely released from terminals as well as somata and dendrites. Based on these findings, we propose that inhibiting APP accumulation in neurons may offer a novel treatment for AD. This proposal is consistent with the recent success of a randomized controlled trial with lecanemab, a monoclonal antibody binding to soluble β-amyloid fibrils, which decisively demonstrated that reduction of soluble β-amyloid lowers amyloid burden as revealed by PET scan and interferes with cognitive deterioration [63]. This is a major breakthrough in AD drug discovery since several large-scale trials with β-amyloid antibodies failed repeatedly or remained controversial [64–66]. One of the key factors that led to their success was the recruitment of persons with early AD for testing. AD progresses gradually over a few decades, starting with sequential preclinical events and finally manifesting clinical dementia [67,68]. Soluble β-amyloid is formed at an early stage of such AD pathogenesis. Our proposed APP lowering may have an advantage since it can be started at an even earlier stage, wherein soluble β-amyloid is not yet generated, but its precursor protein APP is accumulated. Then, the knowledge of the intra-neuronal metabolism of APP should be of great importance. However, how APP is metabolized and β-amyloid is produced and released in neurons is still controversial [20,44,69,70], and resolving this issue should be necessary to determine where AD drugs can be effectively targeted. Since some APP_{SWE}-positive neuronal pathways appear sequentially segregated in the brain of 3xTg-AD mice (e.g., hippocampus to septum) due to the restricted distribution of APP_{SWE} expression in the brain, 3xTg-AD AD model mice could be useful for investigating the neuronal mechanism of β-amyloid generation and release in vivo.

Funding

This work was supported by grants from the Japan Society for the Promotion of Science KAKENHI Grant JP16K11200 (for MO), 23H03243 (for TI), 23H04342 (for TI), 21K11251 (for SY), 17H02223 (for NK), 22K09734 (for NK), 21K07489 (for RY), 22K15795 (for TF), JST FOREST Program JPMJFR2151 (for TI), a Grant from Kieiotoyo Foundation (for NK), a Grant from Smoking Research Foundation (for TI), a Grant from Shibuya Science Culture and Sports Foundation (MO), a Grant from the Naito Foundation (TF), a Grant for Promoted/Collaborative Research from Kanazawa Medical University S2016-8 (for MO), C2018-1 (for NK) and C2022-3 (for RY).

Data availability statement

The data in this study will be available from the corresponding author upon reasonable request.

Submission declaration and verification

This work has not been published previously. It is either not under consideration for publication elsewhere. Its publication is approved by all authors and responsible authorities where the work was done. If accepted, it will not be published in the same form, in English or in any other language, including electronically without the written consent of the copyright-holder.

CRediT authorship contribution statement

Munenori Ono: Writing – review & editing, Writing – original draft, Visualization, Supervision, Software, Methodology, Investigation, Funding acquisition, Formal analysis, Conceptualization. **Tetsufumi Ito:** Writing – review & editing, Visualization, Software, Methodology, Investigation, Funding acquisition, Conceptualization. **Sachiko Yamaki:** Investigation, Funding acquisition. **Yoshie Hori:** Investigation. **Qing Zhou:** Investigation. **Xirun Zhao:** Investigation. **Shinji Muramoto:** Investigation. **Ryo Yamamoto:** Writing – review & editing, Investigation, Funding acquisition. **Takafumi Furuyama:** Writing – review & editing, Investigation, Funding acquisition. **Hiromi Sakata-Haga:** Writing – review & editing, Investigation. **Toshihisa Hatta:** Writing – review & editing, Investigation. **Tsuyoshi Hamaguchi:** Writing – review & editing, Investigation. **Nobuo Kato:** Writing – review & editing, Supervision,

Methodology, Funding acquisition, Conceptualization.

Declaration of competing interest

The authors declare that they have no known competing financial interests or personal relationships that could have appeared to influence the work reported in this paper.

Appendix A. Supplementary data

Supplementary data to this article can be found online at https://doi.org/10.1016/j.heliyon.2024.e28821.

References

[1] P. Scheltens, et al., Alzheimer's disease, Lancet 397 (10284) (2021) 1577–1590.
[2] L. Mucke, D.J. Selkoe, Neurotoxicity of amyloid beta-protein: synaptic and network dysfunction, Cold Spring Harb Perspect Med 2 (7) (2012) a006338.
[3] G.F. Chen, et al., Amyloid beta: structure, biology and structure-based therapeutic development, Acta Pharmacol. Sin. 38 (9) (2017) 1205–1235.
[4] H. Hampel, et al., The amyloid-beta pathway in Alzheimer's disease, Mol. Psychiatr. 26 (10) (2021) 5481–5503.
[5] J. Andrade-Guerrero, et al., Alzheimer's disease: an updated overview of its genetics, Int. J. Mol. Sci. 24 (4) (2023).
[6] S. Oddo, et al., Triple-transgenic model of Alzheimer's disease with plaques and tangles: intracellular Abeta and synaptic dysfunction, Neuron 39 (3) (2003) 409–421.
[7] K.J. Oh, et al., Staging of Alzheimer's pathology in triple transgenic mice: a light and electron microscopic analysis, Int. J. Alzheimer's Dis. 2010 (2010).
[8] C.R. Overk, C.M. Kelley, E.J. Mufson, Brainstem Alzheimer's-like pathology in the triple transgenic mouse model of Alzheimer's disease, Neurobiol. Dis. 35 (3) (2009) 415–425.
[9] R. Belfiore, et al., Temporal and regional progression of Alzheimer's disease-like pathology in 3xTg-AD mice, Aging Cell 18 (1) (2019) e12873.
[10] J.L. Dennison, et al., Sexual dimorphism in the 3xTg-AD mouse model and its impact on pre-clinical Research, J Alzheimers Dis 80 (1) (2021) 41–52.
[11] A.W. Bero, et al., Neuronal activity regulates the regional vulnerability to amyloid-beta deposition, Nat. Neurosci. 14 (6) (2011) 750–756.
[12] C. Hofling, et al., Differential transgene expression patterns in Alzheimer mouse models revealed by novel human amyloid precursor protein-specific antibodies, Aging Cell 15 (5) (2016) 953–963.
[13] H.W. Dong, et al., Genomic-anatomic evidence for distinct functional domains in hippocampal field CA1, Proc. Natl. Acad. Sci. U. S. A. 106 (28) (2009) 11794–11799.
[14] C.L. Thompson, et al., Genomic anatomy of the hippocampus, Neuron 60 (6) (2008) 1010–1021.
[15] D.W. Dickson, The pathogenesis of senile plaques, J. Neuropathol. Exp. Neurol. 56 (4) (1997) 321–339.
[16] M.A. DeTure, D.W. Dickson, The neuropathological diagnosis of Alzheimer's disease, Mol. Neurodegener. 14 (1) (2019) 32.
[17] P. Cras, et al., Senile plaque neurites in Alzheimer disease accumulate amyloid precursor protein, Proc. Natl. Acad. Sci. U. S. A. 88 (17) (1991) 7552–7556.
[18] H. Braak, E. Braak, Neuropathological stageing of Alzheimer-related changes, Acta Neuropathol. 82 (4) (1991) 239–259.
[19] P. Nuntagij, et al., Amyloid deposits show complexity and intimate spatial relationship with dendrosomatic plasma membranes: an electron microscopic 3D reconstruction analysis in 3xTg-AD mice and aged canines, J Alzheimers Dis 16 (2) (2009) 315–323.
[20] S.R. DeBoer, et al., Differential release of beta-amyloid from dendrite- versus axon-targeted APP, J. Neurosci. 34 (37) (2014) 12313–12327.
[21] G. Feng, et al., Imaging neuronal subsets in transgenic mice expressing multiple spectral variants of GFP, Neuron 28 (1) (2000) 41–51.
[22] C. Porrero, et al., Mapping of fluorescent protein-expressing neurons and axon pathways in adult and developing Thy1-eYFP-H transgenic mice, Brain Res. 1345 (2010) 59–72.
[23] K. Yamamoto, R. Yamamoto, N. Kato, Amyloid beta and amyloid precursor protein synergistically suppress large-conductance calcium-activated potassium channel in cortical neurons, Front. Aging Neurosci. 13 (2021) 660319.
[24] G. Simic, et al., Does Alzheimer's disease begin in the brainstem? Neuropathol. Appl. Neurobiol. 35 (6) (2009) 532–554.
[25] N. Scarmeas, et al., Motor signs during the course of Alzheimer disease, Neurology 63 (6) (2004) 975–982.
[26] K. Murakami, Conformation-specific antibodies to target amyloid beta oligomers and their application to immunotherapy for Alzheimer's disease, Biosci. Biotechnol. Biochem. 78 (8) (2014) 1293–1305.
[27] S.C. Elgin, G. Reuter, Position-effect variegation, heterochromatin formation, and gene silencing in Drosophila, Cold Spring Harbor Perspect. Biol. 5 (8) (2013) a017780.
[28] R. Morris, Thy-1 in developing nervous tissue, Dev. Neurosci. 7 (3) (1985) 133–160.
[29] T. Burrinha, C. Guimas Almeida, Aging impact on amyloid precursor protein neuronal trafficking, Curr. Opin. Neurobiol. 73 (2022) 102524.
[30] U.C. Muller, T. Deller, M. Korte, Not just amyloid: physiological functions of the amyloid precursor protein family, Nat. Rev. Neurosci. 18 (5) (2017) 281–298.
[31] B.L. Tang, Neuronal protein trafficking associated with Alzheimer disease: from APP and BACE1 to glutamate receptors, Cell Adhes. Migrat. 3 (1) (2009) 118–128.
[32] N. Salvadores, C. Geronimo-Olvera, F.A. Court, Axonal degeneration in AD: the contribution of abeta and tau, Front. Aging Neurosci. 12 (2020) 581767.
[33] H. Decker, et al., Amyloid-beta peptide oligomers disrupt axonal transport through an NMDA receptor-dependent mechanism that is mediated by glycogen synthase kinase 3beta in primary cultured hippocampal neurons, J. Neurosci. 30 (27) (2010) 9166–9171.
[34] V. Lacovich, et al., Tau isoforms imbalance impairs the axonal transport of the amyloid precursor protein in human neurons, J. Neurosci. 37 (1) (2017) 58–69.
[35] I.A. Kuznetsov, A.V. Kuznetsov, How the formation of amyloid plaques and neurofibrillary tangles may be related: a mathematical modelling study, Proc. Math. Phys. Eng. Sci. 474 (2210) (2018) 20170777.
[36] C.M. Mazure, J. Swendsen, Sex differences in Alzheimer's disease and other dementias, Lancet Neurol. 15 (5) (2016) 451–452.
[37] L. Russo-Savage, et al., Role of Kalirin and mouse strain in retention of spatial memory training in an Alzheimer's disease model mouse line, Neurobiol. Aging 95 (2020) 69–80.
[38] D.I. Javonillo, et al., Systematic phenotyping and characterization of the 3xTg-AD mouse model of Alzheimer's disease, Front. Neurosci. 15 (2021) 785276.
[39] K.R. Sadleir, et al., Abeta reduction in BACE1 heterozygous null 5XFAD mice is associated with transgenic APP level, Mol. Neurodegener. 10 (2015) 1.
[40] S.E. Perez, et al., Cholinotrophic basal forebrain system alterations in 3xTg-AD transgenic mice, Neurobiol. Dis. 41 (2) (2011) 338–352.
[41] P.Y. Risold, L.W. Swanson, Connections of the rat lateral septal complex, Brain Res Brain Res Rev 24 (2–3) (1997) 115–195.
[42] C.A. Rizzi-Wise, D.V. Wang, Putting together pieces of the lateral septum: multifaceted functions and its neural pathways, eNeuro 8 (6) (2021).
[43] C.F. Kratochwil, U. Maheshwari, F.M. Rijli, The long journey of pontine nuclei neurons: from rhombic lip to cortico-ponto-cerebellar circuitry, Front. Neural Circ. 11 (2017) 33.
[44] U. Das, et al., Visualizing APP and BACE-1 approximation in neurons yields insight into the amyloidogenic pathway, Nat. Neurosci. 19 (1) (2016) 55–64.
[45] S.W. Oh, et al., A mesoscale connectome of the mouse brain, Nature 508 (7495) (2014) 207–214.

[46] M. Garcia-Alloza, et al., Characterization of amyloid deposition in the APPswe/PS1dE9 mouse model of Alzheimer disease, Neurobiol. Dis. 24 (3) (2006) 516–524.
[47] M.G. Sharoar, et al., Sequential formation of different layers of dystrophic neurites in Alzheimer's brains, Mol. Psychiatr. 24 (9) (2019) 1369–1382.
[48] H. Oakley, et al., Intraneuronal beta-amyloid aggregates, neurodegeneration, and neuron loss in transgenic mice with five familial Alzheimer's disease mutations: potential factors in amyloid plaque formation, J. Neurosci. 26 (40) (2006) 10129–10140.
[49] T. Saito, et al., Single App knock-in mouse models of Alzheimer's disease, Nat. Neurosci. 17 (5) (2014) 661–663.
[50] D.P. Benitez, et al., Knock-in models related to Alzheimer's disease: synaptic transmission, plaques and the role of microglia, Mol. Neurodegener. 16 (1) (2021) 47.
[51] S.S. Jiao, et al., Sex dimorphism profile of Alzheimer's disease-type pathologies in an APP/PS1 mouse model, Neurotox. Res. 29 (2) (2016) 256–266.
[52] M.A. Mifflin, et al., Sex differences in the IntelliCage and the Morris water maze in the APP/PS1 mouse model of amyloidosis, Neurobiol. Aging 101 (2021) 130–140.
[53] A. Sil, et al., Sex differences in behavior and molecular pathology in the 5XFAD model, J Alzheimers Dis 85 (2) (2022) 755–778.
[54] M.J. Callahan, et al., Augmented senile plaque load in aged female beta-amyloid precursor protein-transgenic mice, Am. J. Pathol. 158 (3) (2001) 1173–1177.
[55] D. Zhu, A. Montagne, Z. Zhao, Alzheimer's pathogenic mechanisms and underlying sex difference, Cell. Mol. Life Sci. 78 (11) (2021) 4907–4920.
[56] R. Rahmani, et al., Age-dependent sex differences in perineuronal nets in an APP mouse model of Alzheimer's disease are brain region-specific, Int. J. Mol. Sci. 24 (19) (2023).
[57] L. Wang, et al., Cognitive recovery by chronic activation of the large-conductance calcium-activated potassium channel in a mouse model of Alzheimer's disease, Neuropharmacology 92 (2015) 8–15.
[58] F. Wang, et al., Improvement of spatial learning by facilitating large-conductance calcium-activated potassium channel with transcranial magnetic stimulation in Alzheimer's disease model mice, Neuropharmacology 97 (2015) 210–219.
[59] T.T. Roos, et al., Neuronal spreading and plaque induction of intracellular Abeta and its disruption of Abeta homeostasis, Acta Neuropathol. 142 (4) (2021) 669–687.
[60] R. Mabrouk, P.O. Miettinen, H. Tanila, Most dystrophic neurites in the common 5xFAD Alzheimer mouse model originate from axon terminals, Neurobiol. Dis. 182 (2023) 106150.
[61] K. Willen, et al., Abeta accumulation causes MVB enlargement and is modelled by dominant negative VPS4A, Mol. Neurodegener. 12 (1) (2017) 61.
[62] D.R. Thal, et al., The development of amyloid beta protein deposits in the aged brain, Sci. Aging Knowl. Environ. 2006 (6) (2006) re1.
[63] C.H. van Dyck, et al., Lecanemab in early Alzheimer's disease, N. Engl. J. Med. 388 (1) (2023) 9–21.
[64] S. Ostrowitzki, et al., A phase III randomized trial of gantenerumab in prodromal Alzheimer's disease, Alzheimer's Res. Ther. 9 (1) (2017) 95.
[65] L.S. Honig, et al., Trial of solanezumab for mild dementia due to Alzheimer's disease, N. Engl. J. Med. 378 (4) (2018) 321–330.
[66] J.L. Cummings, et al., ABBY: a phase 2 randomized trial of crenezumab in mild to moderate Alzheimer disease, Neurology 90 (21) (2018) e1889–e1897.
[67] R.J. Perrin, A.M. Fagan, D.M. Holtzman, Multimodal techniques for diagnosis and prognosis of Alzheimer's disease, Nature 461 (7266) (2009) 916–922.
[68] C.R. Jack Jr., et al., Tracking pathophysiological processes in Alzheimer's disease: an updated hypothetical model of dynamic biomarkers, Lancet Neurol. 12 (2) (2013) 207–216.
[69] L. Fourriere, P.A. Gleeson, Amyloid beta production along the neuronal secretory pathway: dangerous liaisons in the Golgi? Traffic 22 (9) (2021) 319–327.
[70] E.D. Niederst, S.M. Reyna, L.S. Goldstein, Axonal amyloid precursor protein and its fragments undergo somatodendritic endocytosis and processing, Mol. Biol. Cell 26 (2) (2015) 205–217.